2022-8

Optimization of solar-coal hybridization for low solar augmentation

Aaron T. Bame
Brigham Young University - Provo

Joseph Furner
Brigham Young University - Provo

Ian Hoag
PacifiCorp

Kasra Mohammadi
University of Utah

Kody Powell
University of Utah

See next page for additional authors

Original Publication Citation

Bame, A. T., Furner, J., Hoag, I., Mohammadi, K., Powell, K., and Iverson, B. D., 2022, "Optimization of Solar-Coal Hybridization for Low Solar Augmentation," Applied Energy, Vol. 319, pp. 119225. DOI: 10.1016/j.apenergy.2022.119225

Optimization of Solar-Coal Hybridization for Low Solar Augmentation

Aaron T. Bame[a], Joseph Furner[a], Ian Hoag[b], Kasra Mohammadi[c], Kody Powell[c], *Brian D. Iverson[a]

[a]*Brigham Young University, Provo, UT, 84602*
[b]*PacifiCorp, Salt Lake City, UT, 84116*
[c]*University of Utah, Salt Lake City, UT, 84112*

Abstract

This work presents a process to determine the preliminary optimal configuration of a concentrating solar power-coal hybrid power plant with low solar augmentation, and is demonstrated on a regenerative steam Rankine cycle coal power plant in Castle Dale, UT, USA (average DNI of 542 W m^{-2}). A representative plant model is developed and validated against published data for a coal power plant. The simplifications that lead to the representative model from a coal power plant model include combining multiple feedwater heaters, combining turbines, and using a mass-average calculation for extraction steam properties. Comparing net power generation and boiler heating estimates from the representative model to the benchmark power plant, the representative model predictions are accurate to within ± 2.5% of the accepted value. Methods for quantifying solar resource based on geography and simulating a concentrating solar power field arrangement are provided and the solar contribution to electrical power output is estimated using an exergy balance. A financial model is also included to estimate the solar marginal levelized cost of electricity and payback time using a cash-flow analysis. A multi-objective optimization routine is then employed to determine the optimal configuration using the models described in this study.

*Brian D. Iverson
Email address: bdiverson@byu.edu (*Brian D. Iverson)

It is shown that a solar augmentation of >3% of boiler heating is required for a hybrid design to be considered thermodynamically feasible. However, as the augment fraction is increased, the financial benefit from fuel savings is insufficient, without a carbon tax, to offset the higher capital cost. Optimization results, constrained to a maximum solar field size of 20 ac, are also provided assuming a common carbon tax value (16 USD sh.tn.$^{-1}$). The resulting optimal design for the Castle Dale Plant with a carbon tax and no premium indicates the use of parabolic trough collector technology at an augment fraction of $k = 9\%$ to bypass feedwater heater 6. The resulting marginal solar levelized cost of electricity is 9.5 x 10^{-4} USD kWh^{-1} with an estimated payback time of 25.2 years. With a green energy premium price of 0.018 USD kWh^{-1} and no carbon tax, the payback time reduces to 3.9 years. This process can be applied to a subcritical Rankine cycle coal power plant for which operating data and meteorological data are available to evaluate preliminary hybridization feasibility.

Keywords: Hybridization, Concentrating solar power, Coal, Augmentation, Renewable energy

---

Acronyms

BFP	Boiler Feed Pump
BFPT	Boiler Feed Pump Turbine
CC	Capital Cost
CO_2	Carbon Dioxide
CP	Condensate Pump
CSDNI	Clear Sky Direct Normal Insolation [W m^{-2}]
CSP	Concentrating Solar Power
DA	Deaerator
DC	Drain Cooler
DNI	Direct Normal Insolation [W m^{-2}]
EPRI	Electric Power Research Institute
FE	Fuel Earnings [USD]

FS	Fuel Saving
FWH	Feedwater Heater
GHG	Greenhouse Gas
HP	High Pressure
HPT	High Pressure Turbine
HTF	Heat Transfer Fluid
IPT	Intermediate Pressure Turbine
ISCC	Integrated Solar Combined Cycle
LCOE	Levelized Cost of Electricity [USD kWh^{-1}]
LFR	Linear Fresnel Reflector
LP	Low Pressure
LPT	Low Pressure Turbine
NG	Natural Gas
NREL	National Renewable Energy Laboratory
NSRDB	National Solar Resource Database
O&M	Operation & Maintenance
OBJ	Objective
PB	Power Boost
PBT	Payback Time [years]
PTC	Parabolic Trough Collector
PV	Photovoltaic
PVT	Photovoltaic-Thermal
SAM	System Advisor Model
SCA	Solar Collection Assembly
SI	Solar Integration
SX	Solar Exchange
TES	Thermal Energy Storage

Variables

$\dot{Q}_B$	Boiler Heating Power [MW]

$\dot{Q}_{\text{fo}}$	Thermal Equivalent of Fuel Offset [MW]
$\dot{W}$	Mechanical Power [MW]
η	Efficiency [%]
η_c	CSP Collection Efficiency [%]
η_{su}	Solar Use Efficiency [%]
η_{th}	Thermal Efficiency [%]
η_{II}	2^{nd} Law Efficiency [%]
ω	Optimization Objective Weight [-]
A	Area [m^2]
C	Cost [USD]
$c_{p,s}$	Specific Heat of Solar Heat Transfer Fluid [kJ kg^{-1} K^{-1}]
d_r	Receiver Diameter [m]
E	Total Energy [kWh]
F	Conversion Factor
f	Optimization Objective [kW^{-1}]
h	Specific Enthalpy [kJ kg^{-1}]
h_{sun}	Useful Solar Time [hours day^{-1}]
k	Augment Fraction [%]
L	Length [m]
$\dot{m}$	Mass Flow Rate [kg s^{-1}]
m_{ef}	Mass Extraction Fraction [ ]
N_l	Number of Solar Field Loops
N_a	Number of Solar Collection Assemblies per Loop
P_{s1}	HPT 1^{st} Stage Pressure [MPa]
r	Rate or Ratio
s	Specific Entropy [kJ kg^{-1} K^{-1}]
T	Temperature [K]
T_0	Dead State Temperature [K]
W_p	Aperture Width [m]
$\dot{X}$	Exergy Rate [kW]

Subscripts

$[\,]_c$	Concentration Property
$[\,]_d$	Discount Property
$[\,]_n$	Annual Value
$[\,]_p$	Aperture Property
$[\,]_r$	Solar Receiver Property
$[\,]_s$	Solar Field/Solar Contribution
$[\,]_{\text{net}}$	Net Property
$[\,]_{\text{opt}}$	Optimum Property

Financial Variables (Appendix B)

A	Cumulative Cash Flow
FCR	Fixed Charge Rate
DC	Direct Costs
C_{exp}	Operation and Maintenance Expenses
C_{FOM}	Fixed Operation and Maintenance Costs
C_{ins}	Insurance Costs
$C_{P\&I}$	Principle and Interest Payment
$C_{t,\text{prp}}$	Property Tax Costs
C_{VOM}	Variable Operation and Maintenance Costs
CFF	Construction Factor
CRF	Capital Recover Factor
EPC	Engineering-Procurement-Construction
F_L	Debt Fraction
FS	Fuel Savings
IC	Indirect Costs
IRR	Internal Rate of Return
ITC	Investment Tax Credit
$L_{\text{net},0}$	Initial Loan Balance

N_L	Loan Period
PFF	Project Factor
PTC	Project Tax Credit
r_d	Discount Rate
r_i	Inflation Rate
r_{int}	Loan Interest Rate
S	Savings
SC_{dep}	Depreciation Schedule
WACC	Weighted Average of Component Costs
$[\,]_{\text{an}}$	Annual
$[\,]_{\text{con}}$	Construction
$[\,]_{\text{cont}}$	Contingency
$[\,]_{\text{Fed}}$	Federal
$[\,]_{\text{nom}}$	Nominal
$[\,]_r$	Real
$[\,]_{\text{sal}}$	Sales
$[\,]_{\text{SI}}$	Site Improvements
$[\,]_{\text{st}}$	State
$[\,]_t$	Tax

1. Introduction

Concerns with fossil fuels have sparked an ongoing debate, the result of which has been the dramatic increase in power generation using renewable resources. Increases in power generation from solar and wind during 2018-2019 were 140 and 100 trillion BTU, respectively [1]. At first glance, renewable plants seem to solve problems associated with fossil fuels in that the resources are naturally occurring, renewable, and the process for the conversion of the energy to useful power does not provide harmful emissions. However, renewable energy systems often suffer from high capital costs [2] and intermittency [3] which can preclude the penetration of renewable energy systems into many markets.

One solution proposed in 1975 [4] and further explored in 1993 [5] is to break out of the fossil-renewable dichotomy and implement hybrid power plants. The source energy for hybrid power plants may be either predominantly fossil-fuel with renewable augmentation or predominantly renewable with fossil-fuel augmentation. The integration of renewable and fossil fuel sources is able to maintain the necessary energy supply when the renewable resource availability drops while also reducing the amount of carbon-based fuel used with the associated emissions.

Concentrating solar power (CSP) augmentation of coal power plants offers multiple benefits including a reduction of CO_2 with some of the energy resource coming from a renewable source, a reduction in the overall cost as compared to a stand-alone CSP plant of the same combined capacity, and an increase in availability and capacity relative to a stand-alone CSP plant [6]. CSP hybrid power plants have been shown to have greater solar-to-electric efficiency than stand-alone CSP power plants by 10% [7] up to 26% [8], and that plant-level integration is superior to grid-level integration [9]. CSP integration also results in improved ramping time [10], higher solar-to-electric efficiency, reduced costs for retrofitted projects, and higher capacity factors without thermal energy storage [11]. Among the various possible applications of CSP hybridization [12], coal is a popular candidate because CSP and coal share many of the same power

generation components and because of the large presence of coal throughout the world. However, the possibility of hybridization is affected by more than just thermodynamic performance [13].

Zhai et al. [14] studied the life cycle of nine power plant combinations for baseload coal, CSP hybrid, and CSP hybrid with thermal energy storage (TES) at 300, 600, and 1000 MW outputs. Each configuration was evaluated from plant construction to the end of the expected life on a weighted sum of objective scores: (1) global warming potential, (2) acidification potential, (3) respiratory effects potential, (4) primary energy consumption, and (5) capital costs. Zhai et al. showed that for each objective value, every hybrid plant performs better than a coal-fired plant with one exception, capital costs. This means that, when considering hybridization potential, as capital costs become more important and other economic factors such as carbon tax are neglected, hybrid viability decreases.

Manente studied the benefits of hybridization and demonstrated which plant modifications and mode (power boost versus fuel saving) would provide an increase of 50 MW_e [15]. The power boost configurations (in which solar augmentation is used to increase the power generation holding fuel consumption constant) were shown to be most beneficial for newly constructed power plants. Fuel saving modes (in which solar augmentation is used to hold power generation constant and decrease fuel consumption) were evaluated for configurations that required no equipment changes (FS1) and for the case of an upgraded turbine (FS2). Upgrading the turbine allowed the plant to meet the goal of +50 MW_e power boost. Although the FS1 condition required slightly more augmentation than power boost conditions, it provided a greater power boost and higher solar radiation-to-thermal efficiency. The power boost capabilities of hybrid plants are further demonstrated in Wang et al. where several configurations of both solar tower and parabolic trough collectors are shown to result in an increase in annual power generation as compared to the baseline power plant [16].

Hybrid performance is also affected by the fossil-fueled power station to which the renewable plant is attached and the amount of solar energy used, as

shown in Huang et al. [17]. Results suggest that hybridization is feasible when the baseline plant output is greater than 300 MW. It is also shown that for plant power ratings greater than 300 MW, there is an optimal augment fraction to minimize the levelized cost of electricity (LCOE).

Studies into flexible heat generation have shown the benefits of alternating the integration of solar thermal energy from CSP collection into a fossil fuel power plant based on the amount of instantaneous solar resource available between steam generation, steam superheating [18], and feedwater heater (FWH) bypass [19]. Both Behar et al. [20] and Libby et al. [21] suggest that, among other options, solar can be integrated at a FWH where steam, extracted from a turbine, is typically used to preheat some other working fluid. Downstream effects can be mitigated by selecting the augment fraction such that the heat transfer limits of the FWH are not surpassed. This method is known as FWH bypass and has been shown to be a feasible candidate for CSP-coal hybridization [22] when considering financial impacts [23], plants of smaller scales [24], and even when compared with other hybrid technology configurations [6]. Like the integrated solar combined cycles discussed in Manente [15], coal plants can integrate solar thermal energy by means of FWH bypass and operate in FS mode.

Okoroigwe and Madhlopa summarized solar hybrid sites around the world as of 2016 [25]. There are currently 12 CSP hybrid plants throughout the world in operation or under construction, with the addition of the Al-Abdaliyah plant in Kuwait [26], the Waad Al Shamal and Duba 1 plants in Saudi Arabia, and the Dadri plant in India all under construction since Okoroigwe and Madhlopa [27]. All operational plants use parabolic trough collectors (PTC) and offset natural gas with the exception of the Dadri Hybrid Plant in India (under construction) which will be the only hybrid plant in operation to use linear Fresnel reflectors (LFR) and the only plant augmenting coal [28]. Studies demonstrating the use of CSP in integrated solar combined cycles with natural gas show considerable benefits in hybrid performance [29], but a way for developers to evaluate hybrid feasibility has not been explored.

Several studies have demonstrated the process of evaluating hybridization feasibility for specific locations such as Algeria [30], Lebanon [31], Kuwait [26], China [24], Greece [32], and Arabia [33]. However, not all hybrid configurations show a thermodynamic or economic improvemet [34]. The contribution of this study is a generalized CSP-coal hybrid model that can be used to evaluate preliminary hybrid feasibility and parameters such as efficiency, LCOE, and reduction in GHG emissions for any coal power plant with minimal modification. The purpose of this study is to develop and demonstrate a generalized method for evaluating CSP-coal hybrid feasibility based on thermoeconomic performance that can be applied to a coal power plant with feedwater heating and reheating. The representative plant model is validated with available data from two subcritical Rankine cycle coal power plants but may also be applicable to supercritical plants. A representative model of coal power plants is presented and validated by data available in archival literature. The methods of estimating solar resource, solar field size, and financial performance are described. An exhaustive search using thermoeconomic optimization methods are shown with discussion about fitness function development including the calculation of solar contribution ($\dot{W}_s$) to plant power output. The optimization methods are demonstrated using Hunter Unit 3 in Castle Dale, UT, USA as a representative coal power plant. This study focuses primarily on retrofit augmentation projects and is most related to fuel saving mode [15] to reduce the cost and complexity of retrofitting a power plant with solar collectors while still increasing efficiency.

2. Methods

Each coal plant differs somewhat from the next, but several hardware components are common to most power plant configurations. A representative plant model is developed that generally operates in a similar way to most coal plants but with simplifications that make it broadly applicable. The solar exchange (SX) model simulates the collection of solarthermal energy and its transfer into the representative model. The solar integration model developed in this study,

consisting of the representative plant and SX model, assumes the coal plant of interest has at least one FWH in the low pressure (LP) condensate stage and one FWH in the high pressure (HP) feedwater stage. Specific examples are calculated based on data for the Hunter Unit 3 in Castle Dale, UT, USA and validated by data published in archival literature.

2.1. Power Plant Model

Data made available by PacifiCorp on the Hunter Unit performance provides a reliable source to benchmark the representative model introduced in this report. The Hunter power plant has a nominal power generation rate of 511 MW.

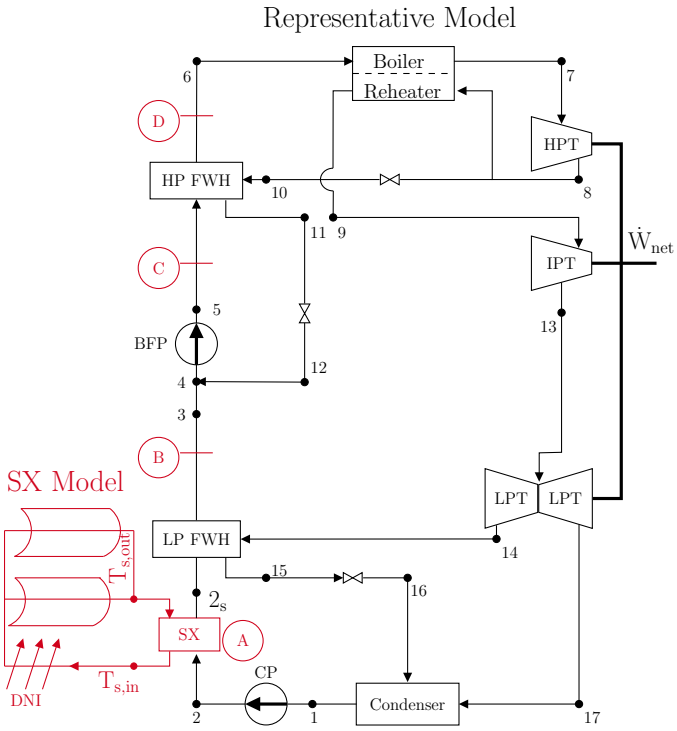

Figure 1: Schematic of the solar integration model consisting of a representative plant model plus a solar exchange (SX) model. Locations for integration of the SX model are illustrated at points A-D and are discussed further in Section 2.3.

The major focus of the plant simplifications center around reducing the number of FWHs as well as the amount of steam and the pressure at which the steam is extracted to run the FWHs. The representative plant model approximates coal power cycles by combining multiple LP and multiple HP FWHs into a single LP FWH run by steam extracted from the low pressure turbine (LPT) and a single HP FWH run by the high pressure turbine (HPT) exhaust. The representative model is shown in Figure 1 in addition to the 4 options for solar integration (A-D), discussed further in Section 2.3.

The FWHs used in the representative plant model are modeled as open FWHs, similar to those found in published articles and in the Hunter heat balance diagram. The drain cooler (DC) is used to fix the operating parameters in the representative plant model and sets the temperature difference between the drain outlet and FWH inlet streams. A mass-averaged approach, explained in the discussion surrounding Figure A.1 (Appendix A), is used to approximate the LP and HP FWH extraction pressures and the LP and HP DC temperature differences.

It is efficient to incrementally heat the feedwater in multiple stages where the temperature of the extracted steam increases alongside the increase in pressure stage. The pressure of the feedwater ideally does not change significantly as it passes through each FWH. Each FWH can then be modeled as a simplified, isobaric heating process. There are changes to the exergy destruction when the feedwater is not heated incrementally by progressively higher temperatures, but the FWHs are modeled as a single heating process.

As noted by Choudhary [35], heat transfer devices (FWHs and boiler) are significant sources of entropy generation, so reducing the number of and operating parameters for the FWHs is expected to have a non-negligible impact on the overall entropy generated in the cycle. This change in entropy generation will be captured in calculations of $\dot{W}_s$.

Another simplification for the representative model is modeling the boiler feed pump turbine (BFPT). The inlet and exhaust pressures of the BFPT are the same as the LPT inlet and exhaust. Rather than modeling a branch from

the IPT exhaust, the amount of steam that would go through the BFPT is sent through the LPT. To compensate for the additional mass going through the LPT, the power required for the boiler feed pump (BFP) is added to the gross work output requirement from the representative model.

A method of calculating extraction steam properties from combined turbines and for combined FWHs is necessary. From the Hunter heat balance diagram and a comparable plant reported in Adibhatla and Kaushik [23], all LP FWHs use extracted steam from the LPT. The steam used for the LP FWH in the representative model should be steam extracted from the LPT. The mass-averaged pressure of the extraction lines in the Hunter plant is used as the extraction pressure in the representative model. More detail about how the mass-average method is applied to calculate the extraction steam pressure is presented in Appendix A.

The HP FWHs in coal plants use varying combinations of steam extracted from both the HPT and IPT. The representative model assumes that the HP FWH uses steam extracted from the HPT exhaust before the reheat process and is throttled to the mass-averaged pressure. The inclusion of the throttling valve adds entropy generation unique to the representative model. Compared to modeling the HP FWH steam as extraction from the IPT in the representative model, throttling the HPT exhaust to the mass-averaged pressure was selected to achieve model accuracy and preserve simplicity.

The efficiency of each turbine is also determined using the mass-averaged approach between the inlet pressure and each extraction and exhaust pressure. The mass-averaged efficiency and the pressures discussed above are sufficient to determine the other fluid properties throughout the cycle. The methods of calculating each individual state point and the inputs needed for the representative model are provided in Appendix A.

Coal power plants control the total power generation of the cycle by adjusting the HPT 1st stage pressure (P_{s1}) and the working fluid mass flow rate. The representative model was modified to calculate the plant performance, limited by a maximum power output constraint, when allowing bypass of a single FWH

by solar heating (i.e. solar bypass). After simulating the turbine power generation with the recalculated extraction pressure, power output constraints for the overall plant and each individual turbine can be compared to the respective calculated values. If a constraint is violated, P_{s1} is incrementally reduced by 5% until all constraints are satisfied.

Changing P_{s1} has downstream effects on the mass flow rate, boiler operating temperature, and pressure ratios between the inlet to a turbine and each respective extraction or exhaust stream. Relationships between P_{s1} and each operating property must be determined and included in the model. Specifically, the properties for which a correlation is required include:

- Condenser pressure
- All FWH extraction pressure ratios
- Boiler inlet pressure
- Boiler outlet pressure
- Boiler operating temperature
- Boiler inlet mass flow rate
- Deaerator (DA) inlet water mass flow rate
- Extraction fractions for each FWH
- HPT, IPT, LPT isentropic efficiencies
- IPT, LPT extraction pressure ratios

Specific correlations for each property listed above are provided in Table A.1 along with a detailed description of how each state point is calculated in Appendix A.

In order to validate the representative model, the power output, boiler heating power, and thermal efficiency were calculated using the representative plant model and compared to data from Hunter Unit 3 and Adibhatla and Kaushik (Table 1) [23].

		$\dot{W}_{\mathbf{net}}$ [MW]	$\dot{Q}_{\mathbf{in}}$ [MW]	η_{th} [%]
Hunter	Reported Cycle Performance	511	1273	37.3
	Representative Model	505	1276	39.6
	Relative Change (%)	-1.2	0.2	6.2
Adibhatla & Kaushik	Reported Cycle Performance	500	1300	38.5
	Representative Model	511	1332	38.3
	Relative Change (%)	2.2	2.5	-0.4

Table 1: Results of applying the representative plant model to the Hunter 3 Unit and the data provided in Adibhatla and Kaushik [23].

The largest error between the representative plant model and data for the Hunter Plant is in the thermal efficiency. This error likely stems from using mass-averaged values and other simplifications listed in this report or from the databases and methods used to calculate steam and water thermodynamic properties. Using mass-averaged values approximates the changes in turbine efficiency with flow rate which affects the reported power output. Assuming constant pressure through FWH stages also reduces the power required by the CP and BFP. However, the net power output error is consistent between the two examples, so altering input parameters, e.g. solar augmentation, should have a consistent effect on the reported net power output. The boiler heating model is more accurate and will closely approximate the heating load on the system and corresponding emissions reduction from solar augmentation.

Analysis of the performance of each turbine provides further insight into the error in net power estimation by the representative model as compared to Hunter Unit 3 (Table 2). Error in the LPT is expected because that process is impacted most by the mass-average process, but the largest error is in the IPT. Using the mass-average approach is expected to cause a large impact on the LPT because it often has the most extraction lines. For the case of the Hunter Unit 3 LPT, the mass-averaged extraction pressure is between the two streams extracted from the LPT at the lowest pressures. Due to this lower mass-averaged

Table 2: Itemized comparison of turbine performance from the representative model to data for the Hunter Unit 3.

	$\dot{W}_{\mathbf{HPT}}$ [MW]	$\dot{W}_{\mathbf{IPT}}$ [MW]	$\dot{W}_{\mathbf{LPT}}$ [MW]
Hunter Unit 3	145	111	255
Representative Model	143	103	260
Relative Change (%)	1.4	7.2	-2.0

pressure, the power generated by the streams extracted from higher pressures is over-approximated. One way to improve the accuracy of these power estimates and the plant performance as a whole would be to determine a model for each turbine's isentropic efficiency. In the current study, each turbine's isentropic efficiency was assumed to be constant.

It is important to also note how the representative model compares to Hunter and Adibhatla and Kaushik's data for the entire cycle in addition to the parameters outlined in Table 1. More accurate approximations of the power plant in Adibhatla and Kaushik may be attainable with operating data similar to the data made available for the Hunter Unit 3. Figure 2 shows the comparison of the predicted state points from the representative model with the Hunter Unit 3 (Figure 2a) and Adibhatla and Kaushik (Figure 2b). The representative model sacrifices some accuracy to achieve consistency in modeling power plants with different configurations. Thus, results for this study will be obtained by varying the amount of solar augmentation to produce results that can be compared to each other based on changes in fuel consumption

One notable difference is the discrepancy between the temperature of the mass entering the condenser of the Hunter Unit, located at the bottom right of the cycle diagram in Figure 2a. The data used to define the Hunter Unit main loop is obtained directly from the heat balance diagram. The Hunter operating data suggests the LPT exhaust is actually at a lower pressure than is reported on the diagram. Using experimental data for the LPT exhaust would improve

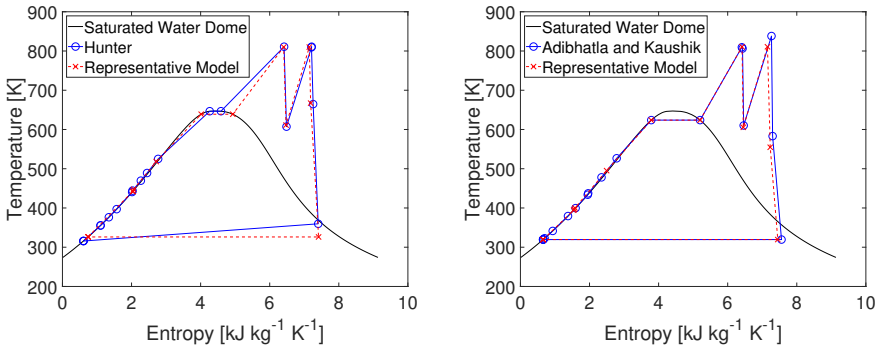

(a) (b)

Figure 2: T-s diagrams comparing the performance of the representative model with (a) Hunter 3 Unit and (b) data in Adibhatla and Kaushik [23].

the Hunter comparison in Figure 2a.

Another discrepancy is the separation between the Hunter data and representative model (Figure 2a) in the heat addition process. This is due to a difference in boiler inlet pressures. The data plotted for the Hunter plant is taken from the plant's heat balance diagram, representing the nominal design conditions for the power plant. The value used for the representative model is calculated using a correlation to the plant's operating data (discussed in Section 2.1). Because the plant doesn't always operate at nominal conditions and correlations have inherent error, some difference in property values is expected.

The error in power output can be seen in Figure 2 by the space between the vertical lines on the far right of each diagram denoting the IPT and LPT processes. As noted above, the error in estimates of power generation is expected when mass-averaged values are used for efficiencies. The $\dot{W}_{\text{net}}$ error is compounded as the same method of using mass averaged values is applied to all turbines. However, the actual plant and respective model diagrams match well and appear to be consistent, regardless of plant configuration.

2.2. Solar Resource

The amount of solar resource available per unit area is referred to in this study as the direct normal insolation (DNI). Since DNI is susceptible to fluctuations due to weather, the maximum possible DNI for a given time is based on calculations for a clear sky (CSDNI), such that DNI≤CSDNI. The following sections describe methods to estimate the expected DNI at any given geography and the use of DNI in the SX model.

The National Renewable Energy Laboratory (NREL) reports solar resource data for a number of locations in the United States, Canada, and South America in the National Solar Resource Database (NSRDB) [36]. Sengupta et al. describes the method of retrieving data from the online NSRDB data viewer in depth [37]. The NSRDB has data from several meteorological measurements. For the methods to evaluate solar resource availability, DNI [W m^{-2}], CSDNI [W m^{-2}], solar zenith angle (θ_z) [degrees], temperature [°C], and pressure [mbar] are utilized.

A MATLAB script has been written to process data downloaded from the NSRDB as described below. The average DNI for each day is calculated according to Equation 1 where N is the number of possible daylight data points. N is determined for each day by counting the number of data points for which CSDNI>0.

$$\mathrm{DNI_{avg}} = \frac{1}{N}\sum_{i=1}^{N}\mathrm{DNI}_i \tag{1}$$

The MATLAB operation uses the average from each day to compute a yearly average and then calculates the average across all years for which data is provided (multi-year average).

For Castle Dale, UT, USA, the calculated multi-year average DNI and daylight time are 542 W m^{-2} and 11.9 h, respectively. The calculated value for multi-year average solar energy then is 6.45 kWh m^{-2}. The NSRDB reports 6.48 kWh m^{-2} as the nominal energy flux value for Castle Dale, UT, USA. The calculated error then is 0.5% of the reported value by NREL. This multi-year average accounts for days of varying solar resource strength and useful time. For

Table 3: Typical dimensions for one PTC or LFR module used in power plants currently in operation [41].

Technology	d_r [m]	W_p [m]	r_c	L_r [m]
PTC	0.08	5.6	20	10
LFR	0.08	15	60	10

the steady state application in this study, it is assumed that the solar resource is available at the multi-year average DNI for a duration of the multi-year average solar time (h_{sun} [hrs day^{-1}]).

PTC and LFR are both categorized as line-focusing CSP technology because they use mirrors to focus the solar irradiation onto a linear receiver. While the performance of LFR systems are comparable with PTC [38], PTC has had the benefit of design improvements and reduction in equipment costs over a longer period. While it has been shown that the performance of PTC exceeds that of LFR in hybrid systems [39], LFR is included in this analysis as a secondary feasible hybrid design option.

Translating the multi-year average DNI to useful energy in the SX model requires sample values for solar collection technology equipment including the diameter and length of a single receiver tube (d_r, L_r), the aperture width (W_p) and corresponding concentration ratio (r_c). Values used for this study are presented in Table 3 and are found from information provided on the NREL SolarPACES site [40].

A solar collection assembly (SCA) is the assembly of multiple modules in series. The projected solar field size is calculated by iterating through different SCA array configurations as described in the development of Equation 5.

The heat transfer fluid selected for this analysis is based on the range of typical temperatures expected in FWHs of the coal power cycle. Increased performance has been shown for advanced LFR with solar salts as the heat transfer fluid [42], but the capital costs associated with this design may critically hinder the feasibility of LFR hybridization. Vignarooban et al. performed an

extensive study on heat transfer fluids available for CSP systems [43]. The data in Vignarooban et al. suggests that a thermal oil is the ideal choice for the design points in this study. Therminol-VP1 is selected for analysis in this study due to the reported stability of Therminol-VP1 and thermal properties at typical CSP operating temperatures for FWH bypass [44].

It is also important to simulate the layout of the solar field to estimate the amount of land used for hybridization. The amount of energy contributed by the solar field is dictated by the augment fraction (k), defined as the ratio of solar energy input to coal energy input to the coal power plant $\left(k = \dot{Q}_s/\dot{Q}_B\right)$.

The solar power received by the coal plant ($\dot{Q}_s$) is dependent on the effectivness (ϵ) of the heat exchanger between the solar receiver power ($\dot{Q}_r$) and the power plant.

$$\dot{Q}_s = \epsilon \dot{Q}_r \tag{2}$$

The performance of the collection technology can be quantified using a collection efficiency (Equation 3), where A_r is the total solar field receiver area and η_c is the overall collection efficiency determined by the technology and estimated operating temperature for PTC [45] and LFR [42].

$$\eta_c = \frac{\dot{Q}_s}{\text{DNI } r_c A_r} \tag{3}$$

The total required length of receiver tube can be determined by combining Equations 2 and 3 with the equation for the surface area of a cylindrical receiver tube [46].

$$L_{min} = \frac{\dot{Q}_s}{\text{DNI } \epsilon \eta_c r_c \pi d_r} \tag{4}$$

For an assumed SCA length of 30 m, the minimum number of required SCA to meet the specifications set by k is the ratio of L_{min} to L_{SCA}, rounded up to the nearest whole assembly.

In order to simplify the calculation of solar energy collection, it was assumed that SCAs are installed in a rectangular array with multiple loops of uniform

length. Consistent with commercial CSP projects and a study published by Channiwala and Ekbote, it was assumed that each loop is installed with a pitch of $L_s = 15$ m between each receiver tube [47]. Since LFR does not require spacing for shading, an additional 5 m (s.t. $L_s = W_p + 5\text{m}$) is added between loops to ensure maintenance access.

The number of SCA required according to Equation 4 is rounded up as necessary to achieve complete rectangular arrays. Using the total surface area of the receiver tube in Equation 4 leads to an underestimation of required area which is partially accounted for in rounding up to achieve rectangular arrays. The resulting calculation of total solar field size (Equation 5) is dependent on the number of SCA in each loop of the array (N_a) and the number of loops in the array (N_l).

$$A_t = (L_r N_a)[W_p N_l + (L_s - W_p)(N_l - 1)] \tag{5}$$

2.3. Solar Exchange

Figure 1 is a sample schematic of the representative model with solar integration in the LP FWH process (Option A). As discussed previously, the representative model used in this study assumes the FWH process is done by a single FWH at constant pressure, so changes are required for property calculations in order to capture the effect of a single FWH being bypassed.

The steam extraction pressure is calculated using the mass-averaged pressure approach assuming all flow rates are unchanged with the exception of the extraction line tied to the bypassed FWH and the main line. In the solar integration model, this is illustrated by placing the solar heat exchanger (SX) in series before the constant pressure FWH (Options A and C in Figure 1) with thermal input from the solar field to the SX if the FWH being bypassed is followed by another FWH in the real cycle. For FWHs not followed by another FWH (i.e. before the boiler or BFP, as in Options B and D in Figure 1), the SX was modeled after the combined FWH in the representative model. State 4 (Figure 1) represents the mixing done in the DA. While the DA may be thought

of as an open FWH, only closed FWHs are considered as candidates for solar integration. However, the FWH numbering scheme common to coal power plant schematics is preserved in this study and FWH 4 is omitted from FWH bypass results discussed in Section 3.

2.4. Solar Contribution

Hou et al. defined a method to calculate the solar work contribution, $\dot{W}_s$, involving an exergy analysis on subsystems of the overall hybrid plant [48]. An adaptation of their approach for the current solar integration model is presented here.

$\dot{W}_s$ is calculated by determining the exergy from the solar field that is converted to usable work. Equation 6 estimates $\dot{W}_s$ from the sum of the solar proportion of work output (r_s) and exergy destroyed (x_d) for the i^{th} subsystem up to N subsystems, the maximum mass flow rate of steam ($\dot{m}_{\max}$), and the exergy transferred from the CSP augmentation (x_s), as follows [48].

$$\dot{W}_s = \frac{1}{1000}\dot{m}_{\max}(x_s - \sum_{i=1}^{N} r_{s,i} \cdot x_{d,i}) \tag{6}$$

Exergy transferred from CSP augmentation is calculated as shown in Equation 7 using the specific enthalpy [h kJ kg^{-1}] and specific entropy [s kJ kg^{-1} K^{-1}] flowing into and out of the solar heat exchanger, T_0, $\dot{m}_m$, and the mass flow rate through the solar heat exchanger ($\dot{m}_{\mathrm{SX}}$) [48].

$$x_s = \frac{\dot{m}_{\mathrm{SX}}}{\dot{m}_m}[(h_{\mathrm{in}} - h_{\mathrm{out}}) - T_0(s_{\mathrm{in}} - s_{\mathrm{out}})] \tag{7}$$

Subsystem boundary lines are selected based on the pressure level of the turbine stage included in the subsystem as shown in Figure 3a with extraction and exhaust pressures. However since steam is not extracted from the IP turbine, the boundary line corresponds with the pressure at state 13. Figure 3b illustrates the boundary lines for each subsystem when plotted on a T-s diagram and shows the highlighted area under the subsystems which is integrated

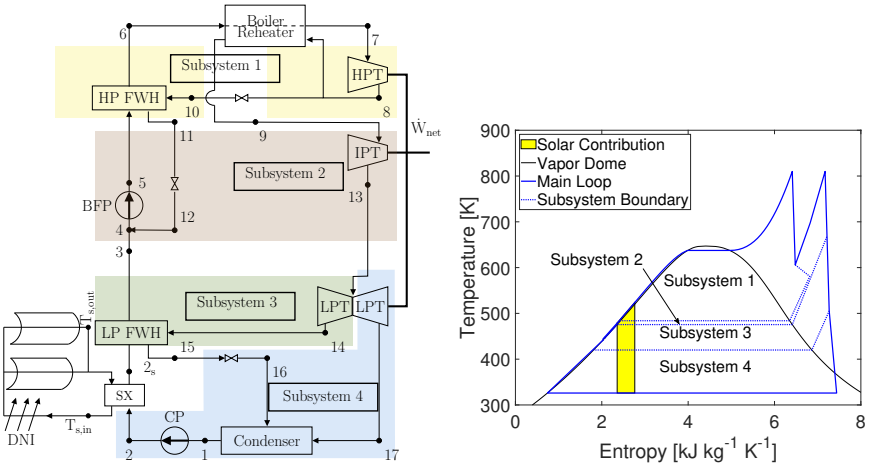

(a) (b)

Figure 3: (a) Subsystem division for LP FWH 1 or FWH 2 bypass and (b) T-s plot of $\dot{W}_s$ for FWH 7 bypass at $k = 1\%$.

to calculate $\dot{W}_s$. Each subsystem remains consistent across multiple solar integration configurations (Options A-D in Figure 1). The only modification is the inclusion of the SX model in different subsystems as the integration location changes. For example, Subsystem 4 always contains the lower stages of the LPT, the condenser, CP, and drain cooler throttling after the LP FWH. For the lowest pressure solar integration (Figure 3a), the SX occurs before LP FWH and splits that boundary between subsystems 3 and 4. Similarly for options B-D, the subsystem boundaries are drawn to exclude the solar integration.

To test the model for $\dot{W}_s$ calculation, the model was compared to the case study by Hou et al. for a 600 MW hybrid plant with FWH 7 bypass, at $k = 5.5\%$ [48]. The study by Hou et al. yielded a $\dot{W}_s$ of 25.70 MW which results in a $\dot{W}_s$ fraction of 4.28%. A similar model presented in this study for FWH 7 bypass at $k = 5.5\%$ and using our representative model yielded a $\dot{W}_s$ of 21.7 MW from a calculated $\dot{W}_{\text{net}} = 494$ MW and $\dot{W}_s$ fraction of 4.4%. With this validation, $\dot{W}_s$ can be used as a parameter to evaluate CSP hybrid performance.

2.5. Financial Model

This study uses an annual cash flow analysis, based on the methods used in the System Advisor Model (SAM) by NREL, to calculate the LCOE and payback time (PBT) based on the time it takes for fuel savings to overcome total project costs. Unless otherwise stated, the equations and values provided for the financial model are retrieved from the SAM documentation [49]. The LCOE calculated from this study is treated as a marginal solar value that can be added to the LCOE of the parent coal plant to estimate the overall hybrid LCOE. The annual cash flow (C_{net}) is calculated (Equation 8) using annual costs (C_n) from operation and maintenance (O&M), financing, and taxes scaled by a nominal discount rate ($r_{d,\text{nom}}$). Input values used to determine C_n are provided in Table 4.

$$C_{\text{net}} = \sum_{n=0}^{N} \frac{C_n}{(1 + r_{d,\text{nom}})^n} \tag{8}$$

Details on the use of the values in Table 4 can be found in Appendix B.

The LCOE is calculated by dividing the annual costs by the annual $\dot{W}_{\text{net}}$, energy (E_n), and adjusting to a net present value (Equation 9), where r_r is the real discount rate.

$$\text{LCOE} = \frac{C_{\text{net}}}{\sum_{n=1}^{N} \frac{E_n}{(1+r_r)^n}} \tag{9}$$

O&M costs, tax costs, and loan payments are approximated using values shown in Table 4, with more information provided in Appendix B.

The PBT used for the current analysis assumes that the fuel savings resulting from operating a hybrid plant in fuel saving mode provide the benefit that offsets all accumulated costs inherent in the hybridization process. The fuel savings are calculated using the fuel offset and the lower heating value of the coal (Equation 10). Annual fuel savings are subtracted from the annual costs

Table 4: Selected input values used for the cash flow cost analysis.

Parameter Name	Variable	Selected Input	Source
	Capital Cost		
Site Improvements	F_{SI} [USD m^{-2}]	25	[49]
Solar Field	F_{SF} [USD m^{-2}]	170	[49]
Heat Transfer Fluid	F_{HTF} [USD m^{-2}]	60	[49]
Heat Exchanger	F_{HX} [MMUSD]	1.73	[50]
Contingency	r_{cont} [%]	7	[49]
Engineer-Procure-Construct	r_{EPC} [%]	11	[49]
Sales Tax Amount	$F_{t,\mathrm{sal}}$ [% of CC]	80	[49]
Sales Tax Rate	$r_{t,\mathrm{sal}}$ [%]	5	[49]
	Annual Operating Expenses		
Fixed O&M	F_{FOM} [USD kW_e^{-1}]	12	[51]
Variable O&M	F_{VOM} [USD MWh^{-1}]	4	[52]
Property Tax Amount	$F_{t,\mathrm{prp}}$ [% of CC]	80	[52]
Property Tax Rate	$r_{t,\mathrm{prp}}$ [% of basis]	0.6	[53]
Insurance Rate	r_{ins} [% of CC]	0.5	[52]
	Annual Loan Payment		
Loan Amount	F_L [% of CC]	50	[54]
Total Loan Period	P [years]	25	[52]
Loan Interest Rate	r_{int} [% of remaining balance]	5	[52]
	Annual Tax Credits and Incentives		
Federal ITC Rate	$r_{\mathrm{ITC,fed}}$ [% of CC]	10*	[55]
State ITC Rate	$r_{\mathrm{ITC,st}}$ [% of CC]	0	[52]
	Annual State and Federal Income Tax		
Depreciation Schedule	$\mathrm{SC}_{\mathrm{dep}}$ [% of CC]	MACRS**	[52]
Federal Tax Rate	$r_{t,\mathrm{Fed}}$ [%]	21	[52]
State Tax Rate	$r_{t,\mathrm{st}}$| [%]	5	[53]

*r_{ITC} was set in 2019 to depreciate from 30% to 10% by 2022 [55].
**The modified accelerated cost recovery system (MACRS) is the name given to the federal depreciation schedule and has a separate value for the first five years of the project as shown in the following vector (20, 32, 19.2, 11.52, 11.52, 5.76).

until the savings are greater than or equal to the cumulative costs.

$$\mathrm{FS} = \frac{E_{sav} F_F}{\mathrm{LHV}_F} \tag{10}$$

The development of this financial model closely reflects the calculations performed within SAM by NREL; comparative tests during development showed agreement between the models on the order of rounding error. Savings obtained from fuel offset is a departure from the scope of SAM. The effect of augmentation and integration site on LCOE and PBT are explored further in Section 3.2.

Carbon tax is an incentive that has been introduced in certain countries and areas of the US to boost renewable energy projects over fossil fuel projects by penalizing the emission of greenhouse gases [56]. Though not widely implemented in the US, hypothetical values for a carbon tax are publicly available [57]. In this work, the effect of the carbon tax income is calculated from $\dot{Q}_{\mathrm{fo}}$ and the useful solar operating conditions. Results from the implementation of a solar premium and carbon tax are provided in Section 3.2.

Another option for improving financial feasibility is the consideration of a premium rate applied to the electricity consumer. A study by O'Shaughnessy et al. states that the average green energy premium paid by residential electricity consumers in 2016 was 0.018 USD kWh^{-1} [58]. In this study, the income from increasing the electricity price for the consumer and the carbon tax are benefits that are treated similarly to income in the calculation. For each year, the premium benefit is calculated from the premium rate and the total energy provided by the power plant during average operating conditions. Alternatively, the green premium can charge the consumer based on the solar contribution to the power generation. Since the $\dot{W}_s$ reported in Table 5 are up to 25 MW for higher k, the effect of the green premium price decreases but the consumer would only be paying for the electricity attributed to the renewable resource.

2.6. Optimization Methods

All models presented to this point comprise the hybrid model. The hybrid model has been designed such that the only inputs, or design variables, required

to calculate hybrid performance are technology type (PTC or LFR), the number of the bypassed FWH, and k. All other model outputs or required inputs are calculated within the hybrid model and are passed between the internal functions as necessary.

Instead of looking at the hybrid plant as a problem with two discrete variables (FWH number and Technology) and one continuous variable (k), the problem can be expanded to be a series of continuous problems resulting in an optimization searching method referred to as an *exhaustive search*. The exhaustive search allows for the optimal configuration to be determined at each integration site in order to find the global optimum for the design space. A study done by Wang et al. showed that there is an optimal augment fraction (k_{opt}) that results in a maximum reduction in fuel consumption [59]. This study uses this phenomenon and similar patterns with other parameters to search for an optimum that considers multiple performance factors.

To implement the exhaustive search, all possible combinations of the discrete variables are treated as individual designs and processed as continuous problems. For the hybrid model, this means that for i possible CSP technologies and j possible integration sites, there will be $i \times j$ continuous optimization problems processed to determine the overall optimum for all possible technology/FWH/k combinations. This exhaustive search is laid out in Figure 4 where each circle is a design variable and each line is a possible value of that variable. Only FWH bypass is considered for this study, so j is equal to the number of closed FWHs. Two feasible CSP technologies are considered: PTC and LFR. Thus, $i = 2$ and $j = 6$ because FWH 4 is an open FWH/deaerator (Section 2.3), and the total number of combinations analyzed is $i \times j = 12$.

The various optimization objectives that have been analyzed in other studies capture important parameters, such as solar to electric efficiency [60], but do not necessarily consider all the factors that impact the overall quality of a design [60–67]. The following parameters have been identified as candidates for the optimization objective. The objective parameters are selected based both on the impact on either thermodynamic or financial performance and the ability

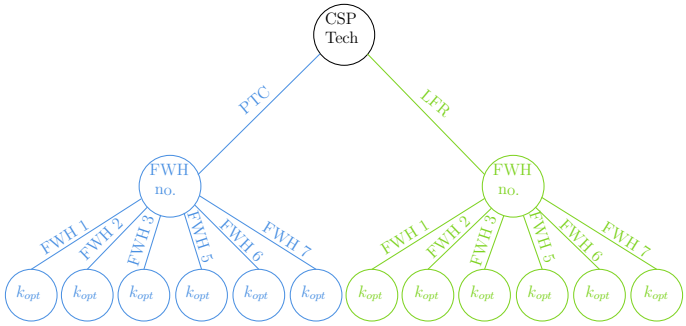

Figure 4: Visualization of the exhaustive search implemented in determining the optimal k (k_{opt}) for each technology/FWH combination.

to maintain consistent dimensions as described below.

- Solar work contribution ($\dot{W}_s$) [MW]
- Fuel offset ($\dot{Q}_{\text{fo}}$) [MW]
- Levelized cost of electricity (LCOE) [USD kWh^{-1}]
- Payback time (PBT) [yrs]
- Fuel earnings (FE) [USD]

The MATLAB function '`fmincon`', included within the MATLAB optimization package, has been selected to perform the continuous search for this study. The models presented in this paper are combined according to the flow diagram in Figure 5 and input to '`fmincon`' which will iterate through differing values of k, FWH, and technology type to find the optimum. Because '`fmincon`' searches for the minimum value of the specified objective, care must be given to combine the variables above such that the ideal value will be a minimum. For best performance, multiple objectives should also have consistent units and be of comparable orders of magnitude.

Objective parameters are separated in two categories based on impact of plant thermodynamics or economics. In this case, objective 1 is defined as $\text{OBJ}_1 = Q_{\text{fo}}\ \dot{W}_s/CC\ \dot{W}_{\text{net}}$, or the maximum amount of fuel saved per dollar spent, and objective 2 is defined as $\text{OBJ}_2 = 1/\text{LCOE}$ (365 PBT h_{sun}), or the minimum amount of money spent on the project. The total objective (f) can then be expressed in terms of the objective parameters (Equation 11) where

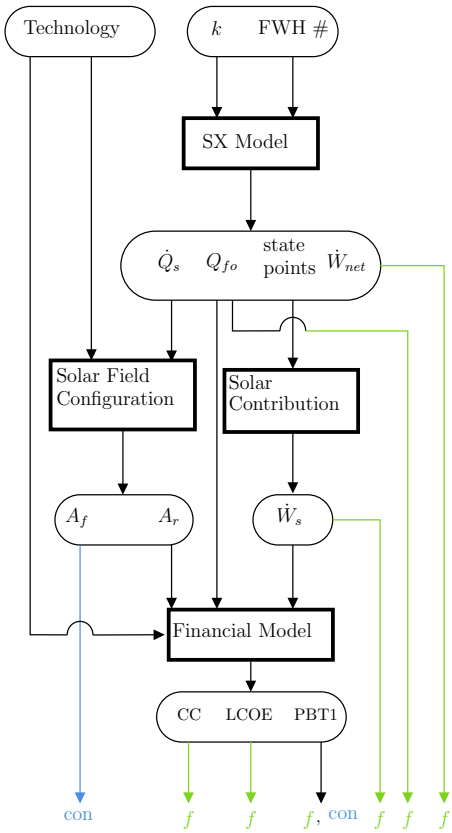

Figure 5: Overview of the interchange of parameters within the hybrid model. Bold rectangles indicate computational models with arrows connecting the necessary inputs and the reported outputs. Input and output variables are contained within rounded rectangles.

each separate objective is scaled by a weight value (ω) such that $\omega_1 + \omega_2 = 1$. The financial parameters are combined to achieve dimensional homogeneity.

$$f = -\omega_1 \frac{\dot{Q}_{\text{fo}}\ \dot{W}_s}{CC\ \dot{W}_{\text{net}}} 10^7 - \omega_2 \frac{1}{\text{LCOE}\ (365\ \text{PBT}\ h_{\text{sun}})} 10^2 \tag{11}$$

Additional constants are multiplied with the objectives as necessary to reach comparable orders of magnitude and dimensional homogeneity, such as converting PBT from years to hours by multiplying 365 days/year and h_{sun}. For best optimization results, the starting point given to '`fmincon`' should be within the

feasible design space.

Additional constraints were placed within the individual models used in the optimization to ensure the outputs were feasible, such as confirming the components within the hybrid model simulation met requirements for the conservation of energy. However, additional constraints are required to ensure the designs generated in the optimization search are feasible for the desired application.

Two additional constraints have been applied restricting the size of the solar field and the duration of PBT. The current optimization constrained the designs to limit the size of the solar field area below a maximum size specified by the user. For this analysis, it is assumed there is an area of 20 ac (81,000 m^2) available for a solar field. A second constraint specifies that the PBT be less than the expected project lifetime specified by the user. A project life of 30 years is assumed for this study.

3. Results

The results presented here are for the models described in Section 2. Unless otherwise specified, the specific values reported and conclusions drawn are based on data for the Hunter Unit 3 coal power plant in Castle Dale, UT, USA.

3.1. Solar Contribution

The methods used to calculate $\dot{W}_s$ were tested for several values of k at each integration site. The energy transferred in each FWH accounts for approximately 3% of the overall heating power done in a coal power plant. Thus, $k = 3\%$ CSP effectively replaces each FWH while providing the same amount of thermal power as the bypassed FWH would and $k = 1\%$ and 6% are used as lower and upper bounds, respectively. Table 5 shows that increasing k and increasing the pressure stage of FWH bypass generally increases $\dot{W}_s$, as expected. Of note is the relative effect of k on $\dot{W}_s$ as compared to integration site. While $\dot{W}_s$ depends on the amount of steam typically extracted from the bypassed FWH, the increase from changing integration site is small as compared to the

increase in $\dot{W}_s$ with increasing k. The choice between k and integration site allows for flexibility in design and operation decisions. Determining the size of a solar field is a decision that must be made in the design stage of a project, but the results in Table 5 suggest that the choice of integration site is much more flexible in that changing the integration from bypassing one FWH to another FWH at a similar pressure stage should not significantly affect the performance of the hybrid plant.

Table 5: Results for solar contribution based on FWH number bypassed and the solar augment fraction (k). Compare with results for $k = 0\%$ in Table 1.

FWH #	$\boldsymbol{k}$ [%]	$\boldsymbol{\dot{W}_s}$ [**MW**]	$\boldsymbol{\dot{Q}_B}$ [**MW**]	$\boldsymbol{\eta_{th}}$ [%]
LP FWH 1	1	1.24	1313	38.6
	3	4.53	1287	38.5
	6	11.42	1276	37.7
LP FWH 2	1	1.24	1293	39.0
	3	4.53	1276	38.8
	6	11.40	1276	37.6
LP FWH 3	1	2.74	1293	39.1
	3	8.88	1263	39.2
	6	18.24	1213	39.2
HP FWH 5	1	3.23	1309	38.7
	3	10.35	1279	38.7
	5	21.97	1233	38.9
HP FWH 6	1	3.23	1299	38.8
	3	10.38	1270	38.9
	5	22.12	1223	39.1
HP FWH 7	1	3.48	1297	37.7
	3	110.4	1267	37.8
	5	24.02	1221	37.9

For the HP configurations that have been shown to be feasible, η_{th} increases

slightly. This behavior was predicted in Section 2.1, though η_{th} is lower than the nominal values reported in Table 1.

3.2. Financial

A sample of financial results is provided in Figures 6 and 7. Of note in Figure 6 is the LCOE order of magnitude. The LCOE reported here is a marginal value representing the ratio of the costs associated only with the integration of CSP to the total hybrid plant energy output. Considering the total LCOE for CSP-coal hybrid systems is on the order of 0.03-0.12 USD kWh^{-1} [27], the marginal fraction reported in this study is a small increase as compared to the LCOE of a total coal or CSP-coal hybrid power plant. This marginal value can then be added to the LCOE of the coal plant to approximate the overall hybrid LCOE. Figure 6 shows that the LCOE depends mainly on k and does not vary considerably for different locations of solar integration in the plant. The general trend for integration options is that the LCOE is less for LP integration.

The fuel offset power ($\dot{Q}_{\text{fo}}$) is the parameter than has the largest effect on PBT. The variation in PBT with k is shown in Figure 7 for HP integration options and 0 USD $sh.tn.^{-1}$ (or short ton) carbon tax. As was shown in Section 2.6, $\dot{Q}_{\text{fo}}$ was negative for FWH 1 and FWH 2 but became positive for all other FWHs once k passed the k_{FWH}. Until $k > k_{\text{FWH}}$, there is no benefit for PBT. However, the costs of the plant continue to increase with k so integration options only become feasible when $\dot{Q}_{\text{fo}}$ gets sufficiently large. The $\dot{Q}_{\text{fo}}$ for HP integration configurations does not vary greatly between each FWH, resulting in nearly identical PBT results for each HP configuration (Figure 7).

Figure 8 shows the effect of carbon tax on the LCOE (Figure 8a) and on PBT (Figure 8b) for FWH 3 and FWH 7 bypass. Values for the carbon tax used to generate Figures 8a and 8b moderate (16 USD $sh.tn.^{-1}$; similar to California Emission Trading System) [56], aggressive (30 USD $sh.tn.^{-1}$; similar to Iceland carbon tax) and very aggressive (50 USD $sh.tn.^{-1}$; France carbon tax) [57]. Even for a moderate carbon tax (16 USD $sh.tn.^{-1}$), significant changes in both LCOE and PBT are seen in Figure 8. This sensitivity to carbon tax suggests that

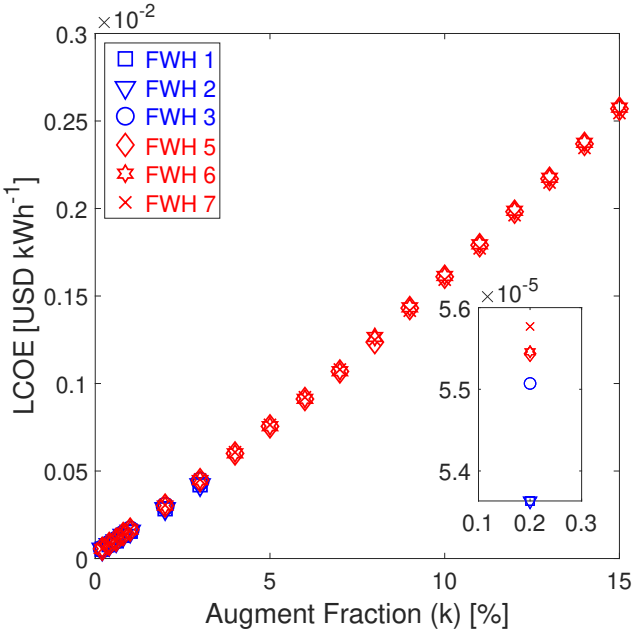

Figure 6: Variation in LCOE with augment fraction, k. The LCOE for each FWH generally increases in the order $1 \approx 2 < 3 < 5 \approx 6 < 7$ as shown in the insert.

hybridization is more likely to have a wider range of feasible designs for locations with carbon taxes in place. Having an LCOE less than 0 (as in Figure 8a) occurs when the financial benefit exceeds the cumulative costs. After the initial investment, the annual net costs must be negative (net financial gain) in order for the project to make money. For projects without carbon tax, the initial investment and annual loan payments are large enough that the summation of each negative LCOE does not make up the difference. With a carbon tax in place, the negative LCOE for each year in the cash flow analysis will increase in magnitude with increasing carbon tax to the point that the summation of negative LCOE for each year surpasses the cumulative LCOE from the initial investment and annual loan payments. In this study, negative LCOE typically corresponds with an aggressive carbon tax or large $\dot{Q}_{\text{fo}}$.

Applying a green energy premium value of 0.018 USD kWh^{-1}, as reported in

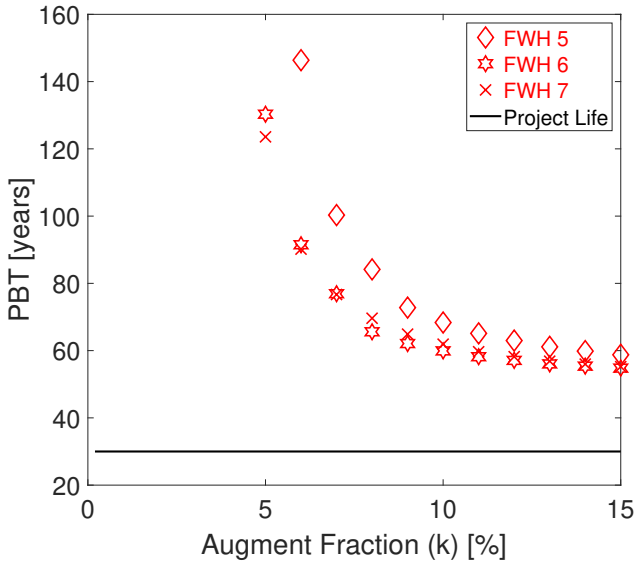

Figure 7: Calculated PBT for solar integration at HP FWHs with 0 USD sh.tn.$^{-1}$ carbon tax. The horizontal line at PBT = 30 years signifies the typical life of coal power plant.

O'Shaughnessy et al. [58], reduces PBT for PTC bypass of FWH 6 at $k = 9\%$ with a 0 USD sh.tn.$^{-1}$ from 62.1 to 3.9 years (94% reduction), resulting in a feasible condition for that k/technology/FWH configuration. As is shown in Figure 9, the PBT with the premium based on $\dot{W}_s$ still decreases but at a lower rate than the PBT with the premium based only on $\dot{W}_{\text{net}}$. For FWH 6 at $k = 9\%$, no carbon tax, and the average green energy premium value of 0.018 USD kWh^{-1}, the PBT comparison from Figure 9 is 3.9 years when based on $\dot{W}_{\text{net}}$ and 22.5 years when based on $\dot{W}_s$.

Consumer electricity rates are highly dependent on location, so the sensitivity of feasibility to green premium price can be seen in Figure 9 for PTC bypass of FWH 6 at $k = 6,\ 9,$ and 10% with a 0 USD sh.tn.$^{-1}$ carbon tax. The main conclusion from Figure 9 is that applying a premium considerably decreases PBT with all else constant. However, there is a limit at which increasing the premium price no longer shows significant decreases in PBT. For Figure 9, the

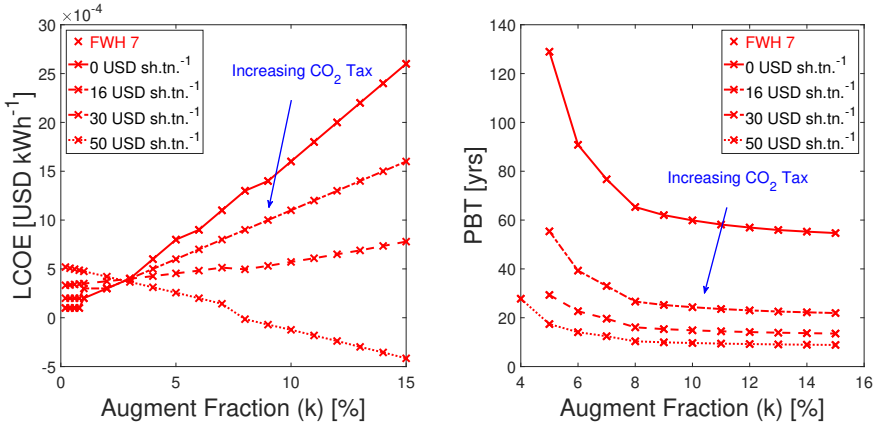

Figure 8: Effect of carbon tax on (a) LCOE and (b) PBT. FWH 6 is used as an example of HP integration. LCOE and PBT trends for other bypass options are similar to those shown in Figures 6 and 7.

change in PBT is less than 2% when it is increased beyond 0.0155 USD kWh^{-1}. The premium of 0.0155 USD kWh^{-1} is sufficient to reduce PBT to 4.3 years for $k = 9\%$.

Looking at the effect of a carbon tax (Figure 8b) and a green premium electricity price (Figure 9) show similar trends in the effect on PBT from carbon tax and green premium. Increasing a carbon tax or green premium will decrease the PBT, but adjusting the green premium has a greater impact than increasing the carbon tax. This is due to how each value is implemented in this study, as discussed in Section 2.5. A carbon tax is applied to the coal saved by solar augmentation, typically as high as 100 MW for low-solar augmentation. The green premium, however, is applied to all the electricity generated during h_{sun} throughout the year. For the Hunter Unit 3 plant with a nameplate generation of almost 500 MW$_e$, the green premium is effectively applied to a greater source of power.

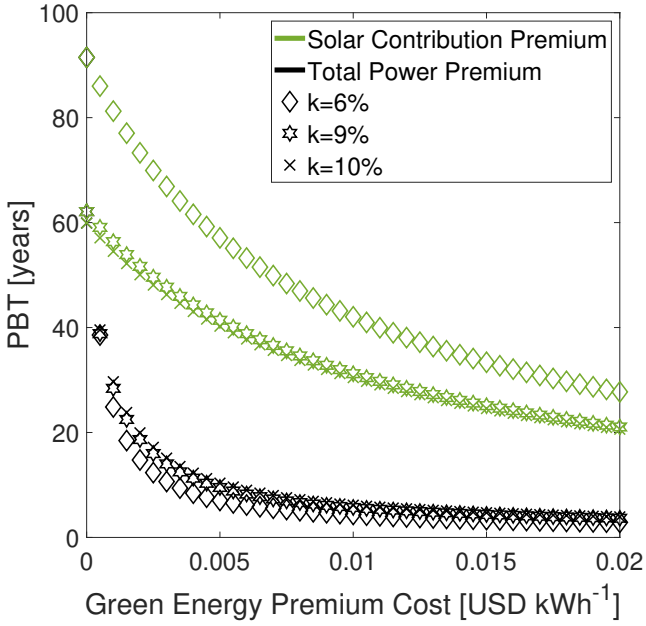

Figure 9: Effect of green premium price and k on PBT.

3.3. Optimization

As described in Section 2.6, hybrid performance is divided in thermodynamic and economic categories. Figure 10 shows the relationship between the two objectives for weights in increments of $\omega = 0.2$ (i.e. $\omega_1 = [0, 0.2, 0.4, \cdots, 1]$, and $\omega_2 = [1, 0.8, 0.6, \cdots, 0]$) for HP FWHs and 16 USD sh.tn.$^{-1}$ carbon tax. The curves represented by the trendlines fit to the calculated optimums are Pareto fronts. The Pareto front for two-objective optimization is a curve that represents the hypothetical boundary for feasible designs. In the case of this study, the optimization objective was written such that the optimal design would trend towards the minimum of each objective. In Figure 10, the Pareto fronts suggest that the majority of other feasible designs result in a higher value for at least one of the two objectives. As expected, the trendline reflects an inverse relationship and the objectives contradict each other. The trendline fit to the sample simulations demonstrates the expected pareto front of feasible designs

for different possible ω combinations. The results in Figure 10 result in the majority of the ω combinations lying closer toward a thermodynamic minimum, suggesting that OBJ1 may be dominating the optimization. In general, the trendline representing the Pareto front for FWH 6 bypass lies below all other designs, suggesting FWH 6 bypass is most likely to be the optimal integration site for a hybrid plant when compared to results for each of the other FWHs.

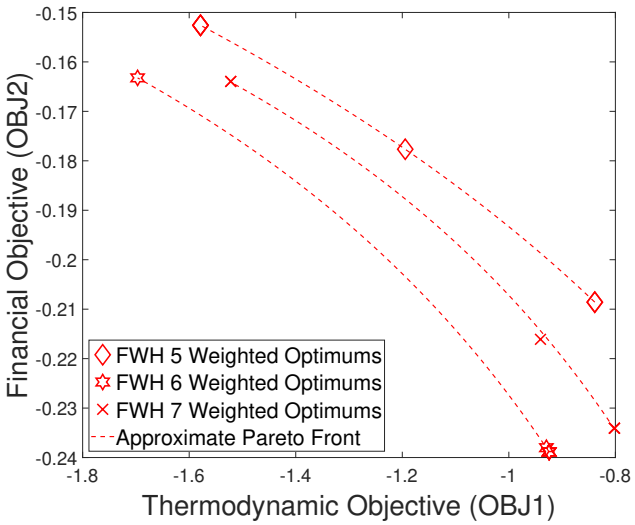

Figure 10: Pareto fronts for HP FWH bypass displaying the competing optimization objectives for the current study and 16 USD sh.tn.$^{-1}$ carbon tax. A minimum in OBJ1 corresponds to a maximum in OBJ2 and vise-versa for each FWH option.

Results from Section 3.2 show that k, directly tied to the capital cost, has the largest impact on financial performance and overall feasibility of a hybrid project once $\dot{Q}_{\text{fo}} > 0$ (Figure 6). Thus, more weight is given to the financial objective, or $\omega_1 = 0.2$, $\omega_2 = 0.8$. Optimization results for each FWH and technology type are given in Table 6 assuming a project life of 30 years and a maximum allowable solar field of 30 ac. As shown in Figure 4, k_{opt} is found for each FWH bypass option combined with either PTC or LFR for the solar field.

The optimization results in Table 6 show the k_{opt} for each technology/FWH combination. The overall hybrid optimal design is found by selecting the con-

Table 6: Optimums for each FWH bypass option for $\omega_1 = 0.2$, $\omega_2 = 0.8$, and 16 USD sh.tn.$^{-1}$ carbon tax. f is a minimizing function, so the smallest value (or most negative) is considered the best.

	FWH #	k_{opt} [%]	$\dot{Q}_{fo}$ [MW]	A_f [ac]	LCOE [10^{-4} USD kWh^{-1}]	PBT [years]	f [kW USD^{-1}]
PTC	5	14.5	202.7	517.9	16	23.7	-0.79
	6	9	112.6	301.4	9.5	25.2	-0.92
	7	9	105.1	301.4	9.6	27.1	-0.84
LFR	5	14.8	208.5	366.5	24	> 30	-0.46
	6	13.2	188.6	320.9	21	> 30	-0.48
	7	14.7	209.2	364.2	23	> 30	-0.46

figuration resulting in the lowest (most negative) value for f (Section 2.6). For this study, $k = 9\%$ PTC bypassing FWH 6 is the optimal configuration for 16 USD sh.tn.$^{-1}$ carbon tax. This result is consistent with similar work published in archival literature suggesting hybrid performance improves as the integration site approaches the boiler stage [68], even when considering financial implications [69]. It was expected that LFR integration would be generally less feasible than PTC due to higher capital costs. This is evident in that none of the optimal designs for LFR had feasible PBT. However, the efficiency of LFR land use is apparent throughout Table 6, but particularly for FWH 5 bypass where the estimated solar field for the LFR configuration is similar to the PTC configuration despite a higher k_{opt} than PTC FWH 5 bypass [70].

3.4. Geography

Changing the geographic location of hybridization also has a significant effect on financial parameters. DNI is highly dependent upon geography, which has a strong impact on the size of the solar field required (Equation 4). Changing location also may change state or federal tax information. As an example of the effect geography has on the optimization results, Table 7 shows the optimal configurations for a plant with parameters consistent with Hunter Unit 3 operating in a city with lower DNI (Cleveland, OH, USA) and a city with higher DNI (El Paso, TX, USA) for FWH 6 bypass and the California carbon tax (16

USD sh.tn.$^{-1}$).

Table 7: Effect of geography on hybrid performance with PTC bypassing FWH 6 with 16 USD sh.tn.$^{-1}$ carbon tax and no green energy premium. Castle Dale, UT is the benchmark with Cleveland, OH and El Paso, TX as examples of lower and upper DNI, respectively (all USA). Local tax and financing parameters are not included.

Location	**DNI**	k_{opt}	A_{sf}	**LCOE**	**PBT**	**f**
	[W m^{-2}]	**[%]**	**[ac]**	**[10^{-4} USD kWh^{-1}]**	**[yrs]**	**[kW USD^{-1}]**
Cleveland, OH	326	14.7	875	30	> 30	-0.35
Castle Dale, UT	542	9	301.4	9.5	25.2	-0.92
El Paso, TX	624	9	263.4	8.0	21.5	-1.26

In comparing the optimization fitness, the minimal f is expected to be in El Paso, TX, USA, depending on the specific operating procedure of a power plant in that area. This confirms the high dependence of CSP technology on installation geography. A proposed hybrid project is most likely to be feasible if the location of interest has high DNI.

The data presented shows that the integration site in the power plant causes the greatest effect on plant performance; k and CSP technology type have the greatest impact on financial performance. Hybridization has an impact beyond just plant efficiency and LCOE.

4. Discussion

The US Energy Information Administration reports that the amount of CO_2 emissions from a coal power plant can be estimated by the conversion factor 205 lb. CO_2 MMBTU^{-1} for bituminous coal [71]. With FWH 6 bypass as an example, Table 6 shows that 52 MW worth of coal is offset during hybrid mode. Using the effective solar time to convert from MW to MMBTU and projecting throughout the year, the conversion from the Energy Information Administration results in a CO_2 emissions reduction of approximately 171 tons per year. According to Bernal et al. [72], a typical temperate, dry conifer forest (the most prominent forest in UT) removes approximately 6.4 t CO_2 ha^{-1} year^{-1}. Thus,

CSP augmentation in UT reduces emissions equivalent to approximately 27,000 ha of dry conifer forest for $k = 9\%$ PTC augmentation at FWH 6 bypass.

This study analyzes a retrofit hybrid model operating in fuel saving mode, but Manente showed that plants constructed with hybrid capabilities, typically operating in power boost mode, can also see considerable benefits [15]. Manente's study, focused on integrated solar combined cycles, shows that the inclusion of solar in the power generation process can add 50 MW_e to an existing plant without changing any equipment. Included in Manente's study was the requirement to upgrade the turbine to account for the potential increase in capacity. This suggests that a power boost analysis is best for initial construction and plants anticipating upgrades to turbines or electrical transformers due to the added capital cost of higher capacity components whereas fuel saving mode is best for retrofit projects.

The impact of hybridization can be extended with the addition of thermal energy storage (TES). Storage technology has been studied for use in building energy efficiency [73] as well as CSP. Common options for storage materials include phase change materials using latent heat [74] or organic materials [75], large collections of rock [76], and molten salts [77]. Studies show that TES can add considerably to the hybridization benefit by stabilizing output [78], improved load management [79], improving economic feasibility [80], and improving revenue opportunities [81]. The inclusion of TES would cause changes in the financial performance of a hybrid plant necessitating edits to the model presented in the current study. The operation of the plant would largely be the same with the exception that the hybrid plant would be able to operate in fuel saving mode for a longer period of time. This increase in effective solar time is expected to increase the total amount of coal saved over time and cause a potential decrease in LCOE and PBT depending on the selection of TES technology.

5. Conclusion

While benefits of hybrid technology have been explored in published literature, this study has contributed a simplified method to evaluate preliminary hybridization feasibility based on a representative coal power plant. The representative model was shown to be applicable to Hunter Unit 3 in Castle Dale, UT, USA and a separate coal power plant with a different configuration [23]. Using solar data from NREL and standard equipment dimensions, the solar resource for the hybrid geography was quantified and combined with the representative model in the solar integration model. The fraction of power out of the hybrid power plant that can be attributed to the solar integration was calculated using an exergy analysis. A financial model was used to calculate comparative parameters including LCOE, PBT, and fuel earnings. The performance of the solar heat exchange model is combined with the financial performance to define the optimization objective used to find the optimal configuration for a proposed hybrid retrofit project. Results from simulating CSP integration into Hunter Unit 3 suggest that hybridization may be feasible considering the expected thermodynamic benefits to the power plant and the LCOE and PBT for small values of k. LFR requires less land for a solar field than PTC, but higher capital costs universally preclude the use of LFR in hybrid projects according to the assumptions of this analysis. As expected, areas with higher average DNI are more promising candidates for $\dot{W}_s$ and areas with lower DNI are less feasibile. It is shown that for a possible scenario including a carbon tax, the LCOE and PBT will decrease accordingly and increase the feasibility of hybridization. The impact of a green premium on consumer electricity prices is also demonstrated to have a dramatic effect on decreasing PBT. Carbon taxes and green premium prices are common in communities across the world [56] and in the US [58], so a combination of both incentives makes CSP-coal hybridization feasible and competitive with other power generation options.

The calculated optimum scenario is using PTC at $k = 9\%$ to bypass FWH 6 with a 16 USD sh.tn.$^{-1}$ carbon tax without considering a green energy premium.

The resulting optimum LCOE and PBT are 9.4×10^{-4} USD kWh^{-1} and 25.2 years, respectively. Applying the green energy premium 0.018 USD kWh^{-1} with no carbon tax reduces the PBT for $k = 9\%$ PTC augment of FWH 6 from 62.1 years with no premium to 22.5 years based only on $\dot{W}_s$ and 3.9 years based on the total power output.

The method presented in this paper, while simplified, is largely irrespective of a particular coal plant, geography, or local tax code. While not explicitly validated for supercritical Rankine cycle coal power plants, this work may be useful in that scenario as well with development. The results suggest a generous range of feasible hybrid configurations, but do not provide an explicit commentary on public policy. While the effects of carbon tax on feasibility as defined in this analysis are substantial, there are many and various effects of carbon tax on an economy and social structure such that this study alone cannot be used to argue for or against the implementation of a carbon tax or other applicable policies. Instead, it is only suggested that hybridization be considered where such policies may be in place.

6. Acknowledgments

Funding is gratefully acknowledged from PacifiCorp. The authors also acknowledge the assistance of Trapper Burdick, Roy Jewkes, and Daniel Kinder for data access, interpretation and understanding.

References

[1] U.S. Energy Information Administration, Annual Energy Review (2020). URL https://www.eia.gov/totalenergy/data/annual/

[2] National Renewable Energy Laboratory, Annual Technology Baseline (2020).
URL https://atb.nrel.gov/electricity/2020/

[3] H. L. Zhang, J. Baeyens, J. Degrève, G. Cacères, Concentrated solar power plants: Review and design methodology, Renewable and Sustainable Energy Reviews 22 (2013) 466–481. doi:10.1016/j.rser.2013.01.032.

[4] R. Zoschak, S. Wu, Studies of the direct input of solar energy to a fossil-fueled central station steam power plant, Solar Energy 17 (5) (1975) 297–305. doi:10.1016/0038-092X(75)90047-X.
URL https://www.sciencedirect.com/science/article/pii/0038092X7590047X

[5] P. De Laquil III, D. Kearney, M. Geyer, R. Diver, Solar-Thermal Electric Technology, in: T. B. Johansson, H. Kelly, A. K. N. Reddy, R. H. Williams (Eds.), Renewable Energy: Sources for Fuels and Electricity, Island Press, Washington, D.C., 1993, Ch. 5, pp. 234–6.
URL https://books.google.com/books?hl=en&lr=&id=40XtqVMRxOUC&oi=fnd&pg=PA1&ots=j0FpG__sTu&sig=71N0R1w_G-lh6MhEs1um3zI_a30#v=onepage&q&f=false

[6] K. M. Powell, K. Rashid, K. Ellingwood, J. Tuttle, B. D. Iverson, Hybrid concentrated solar thermal power systems: A review, Renewable and Sustainable Energy Reviews 80 (2017) 215–237. doi:10.1016/j.rser.2017.05.067.

[7] K. Rashid, M. N. Sheha, K. M. Powell, Real-time optimization of a solar-natural gas hybrid power plant to enhance solar power utilization,

in: 2018 Annual American Control Conference (ACC), 2018, pp. 3002–3007. doi:10.23919/ACC.2018.8431220.

[8] K. Rashid, S. M. Safdarnejad, K. M. Powell, Dynamic simulation, control, and performance evaluation of a synergistic solar and natural gas hybrid power plant, Energy Conversion and Management 179 (July 2018) (2019) 270–285. doi:10.1016/j.enconman.2018.10.054.
URL https://doi.org/10.1016/j.enconman.2018.10.054

[9] K. Rashid, S. M. Safdarnejad, K. Ellingwood, K. M. Powell, Techno-economic evaluation of different hybridization schemes for a solar thermal/gas power plant, Energy 181 (2019) 91–106. doi:10.1016/j.energy.2019.05.130.
URL https://www.engineeringvillage.com/share/document.url?mid=cpx_517f4b9816b6c24c629M5c9e10178163167&database=cpx

[10] Y. Li, Y. Yang, Thermodynamic analysis of a novel integrated solar combined cycle, Applied Energy 122 (2014) 133–142. doi:10.1016/j.apenergy.2014.02.017.
URL http://dx.doi.org/10.1016/j.apenergy.2014.02.017

[11] Y. Zhao, M. Liu, C. Wang, X. Li, D. Chong, J. Yan, Increasing operational flexibility of supercritical coal-fired power plants by regulating thermal system configuration during transient processes, Applied Energy 228 (July) (2018) 2375–2386. doi:10.1016/j.apenergy.2018.07.070.

[12] K. Mohammadi, S. Khanmohammadi, H. Khorasanizadeh, K. Powell, A comprehensive review of solar only and hybrid solar driven multigeneration systems: Classifications, benefits, design and prospective, Applied Energy 268 (March). doi:10.1016/j.apenergy.2020.114940.

[13] A. Ihsan, M. Jeppesen, M. J. Brear, Impact of demand response on the optimal, techno-economic performance of a hybrid, renewable energy power plant, Applied Energy 238 (January) (2019) 972–984.

doi:10.1016/j.apenergy.2019.01.090.
URL https://doi.org/10.1016/j.apenergy.2019.01.090

[14] R. Zhai, C. Li, Y. Chen, Y. Yang, K. Patchigolla, J. E. Oakey, Life cycle assessment of solar aided coal-fired power system with and without heat storage, Energy Conversion and Management 111 (2016) 453–465. doi:10.1016/j.enconman.2015.12.053.
URL http://dx.doi.org/10.1016/j.enconman.2015.12.053

[15] G. Manente, High performance integrated solar combined cycles with minimum modifications to the combined cycle power plant design, Energy Conversion and Management 111 (2016) 186–197. doi:10.1016/j.enconman.2015.12.079.
URL http://dx.doi.org/10.1016/j.enconman.2015.12.079

[16] R. Wang, J. Sun, H. Hong, Proposal of solar-aided coal-fired power generation system with direct steam generation and active composite sun-tracking, Renewable Energy (2019) 596–612doi:10.1016/j.renene.2019.04.013.

[17] C. Huang, H. Hou, E. Hu, M. Liang, Y. Yang, Impact of power station capacities and sizes of solar field on the performance of solar aided power generation, Energy 139 (2017) 667–679. doi:10.1016/j.energy.2017.07.169.
URL https://doi.org/10.1016/j.energy.2017.07.169

[18] K. Ellingwood, K. Mohammadi, K. Powell, A novel means to flexibly operate a hybrid concentrated solar power plant and improve operation during non-ideal direct normal irradiation conditions, Energy Conversion and Management 203. doi:10.1016/j.enconman.2019.112275.
URL https://www.engineeringvillage.com/share/document.url?mid=cpx_5c07ea0816ef02c0a50M732110178163211&database=cpx

[19] K. Ellingwood, K. Mohammadi, K. Powell, Dynamic optimization and economic evaluation of flexible heat integration in a hybrid concentrated

solar power plant, Applied Energy 276 (2020) 115513.
doi:10.1016/j.apenergy.2020.115513.

[20] O. Behar, A. Khellaf, K. Mohammedi, S. Ait-Kaci, A review of integrated solar combined cycle system (ISCCS) with a parabolic trough technology, Renewable and Sustainable Energy Reviews 39 (2014) 223–250.
doi:10.1016/J.RSER.2014.07.066.
URL https:
//www.sciencedirect.com/science/article/pii/S1364032114005188

[21] C. Libby, P. Meagher, L. Cerezo, Solar-Fossil Hybrid Power Plants: Summary Report on Conceptual Designs, 1022418, Tech. rep., Electric Power Research Institute, Palo Alto, CA (2010).
URL www.epri.com

[22] Y. Zhao, H. Hong, H. Jin, Optimization of the solar field size for the solar–coal hybrid system, Applied Energy 185 (2017) 1162–1172.
doi:10.1016/j.apenergy.2016.01.069.

[23] S. Adibhatla, S. C. Kaushik, Energy, exergy, economic and environmental (4E) analyses of a conceptual solar aided coal fired 500 MWe thermal power plant with thermal energy storage option, Sustainable Energy Technologies and Assessments 21 (2017) 89–99.
doi:10.1016/j.seta.2017.05.002.
URL http://dx.doi.org/10.1016/j.seta.2017.05.002

[24] S. Peng, Z. Wang, H. Hong, D. Xu, H. Jin, Exergy evaluation of a typical 330 MW solar-hybrid coal-fired power plant in China, Energy Conversion and Management 85 (2014) 848–855.
doi:10.1016/j.enconman.2013.12.073.

[25] E. Okoroigwe, A. Madhlopa, An integrated combined cycle system driven by a solar tower: A review, Renewable and Sustainable Energy Reviews 57 (2016) 337–350. doi:10.1016/j.rser.2015.12.092.
URL http://dx.doi.org/10.1016/j.rser.2015.12.092

[26] A. O. Binamer, Al-Abdaliya integrated solar combined cycle power plant: Case study of Kuwait, part I, Renewable Energy 131 (2019) 923–937. doi:10.1016/J.RENENE.2018.07.076.
URL https://www.sciencedirect.com/science/article/pii/S0960148118308735

[27] S. Pramanik, R. V. Ravikrishna, A review of concentrated solar power hybrid technologies, Applied Thermal Engineering 127 (2017) 602–637. doi:10.1016/j.applthermaleng.2017.08.038.
URL https://doi.org/10.1016/j.applthermaleng.2017.08.038

[28] M. Sinha, NTPC's Dadri unit set to install solar-thermal hybrid power plant (2017).
URL
https://energy.economictimes.indiatimes.com/news/renewable/ntpc-dadri-set-to-install-solar-thermal-hybrid-plant/57804545

[29] B. J. Alqahtani, D. Patiño-Echeverri, Integrated Solar Combined Cycle Power Plants: Paving the way for thermal solar, Applied Energy 169. doi:10.1016/j.apenergy.2016.02.083.

[30] N. Abdelhafidi, N. E. I. Bachari, Z. Abdelhafidi, A. Cheknane, A. Mokhnache, L. Castro, Modeling of integrated solar combined cycle power plant (ISCC) of Hassi R'mel, Algeria, International Journal of Energy Sector Management 14 (3) (2019) 22. doi:10.1108/IJESM-08-2018-0013.
URL https://www.emerald.com/insight/content/doi/10.1108/IJESM-08-2018-0013/full/html

[31] C. Tannous, D. Ahlam, M. Rosa, Renewable energy integration into existing plants: Application: Deir Ammar thermal plant-North Lebanon, in: 2016 3rd International Conference on Renewable Energies for Developing Countries, REDEC 2016, Institute of Electrical and

Electronics Engineers Inc., 2016, p. 9.
doi:10.1109/REDEC.2016.7577566.

[32] G. C. Bakos, C. Tsechelidou, Solar aided power generation of a 300MW lignite fired power plant combined with line-focus parabolic trough collectors field, Renewable Energy 60 (2013) 540–547.
doi:10.1016/j.renene.2013.05.024Technicalnote.
URL http://dx.doi.org/10.1016/j.renene.2013.05.024

[33] E. M. Mokheimer, Y. N. Dabwan, M. A. Habib, Optimal integration of solar energy with fossil fuel gas turbine cogeneration plants using three different CSP technologies in Saudi Arabia, Applied Energy 185 (2017) 1268–1280. doi:10.1016/j.apenergy.2015.12.029.
URL http://dx.doi.org/10.1016/j.apenergy.2015.12.029

[34] Y. Zhu, J. Pei, C. Cao, R. Zhai, Y. Yang, M. A. Reyes-Belmonte, J. González-Aguilar, M. Romero, Optimization of solar aided coal-fired power plant layouts using multi-criteria assessment, Applied Thermal Engineering 137 (January 2017) (2018) 406–418.
doi:10.1016/j.applthermaleng.2018.03.093.
URL https://doi.org/10.1016/j.applthermaleng.2018.03.093

[35] T. Choudhary, Sanjay, Thermodynamic assessment of SOFC-ICGT hybrid cycle: Energy analysis and entropy generation minimization, Energydoi:10.1016/j.energy.2017.06.064.

[36] National Renewable Energy Laboratory, National Solar Radiation Database (2018).
URL https://maps.nrel.gov/nsrdb-viewer

[37] M. Sengupta, Y. Xie, A. Lopez, A. Habte, G. Maclaurin, J. Shelby, The National Solar Radiation Data Base (NSRDB), Renewable and Sustainable Energy Reviews 89 (2018) 51–60.
doi:10.1016/j.rser.2018.03.003.

[38] H. H. Sait, J. M. Martinez-Val, R. Abbas, J. Munoz-Anton, Fresnel-based modular solar fields for performance/cost optimization in solar thermal power plants: A comparison with parabolic trough collectors, Applied Energy 141 (2015) 175–189. doi:10.1016/j.apenergy.2014.11.074.
URL https:
//linkinghub.elsevier.com/retrieve/pii/S0306261914012434

[39] A. Rovira, R. Barbero, M. J. Montes, R. Abbas, F. Varela, Analysis and comparison of Integrated Solar Combined Cycles using parabolic troughs and linear Fresnel reflectors as concentrating systems, Applied Energydoi:10.1016/j.apenergy.2015.11.001.

[40] National Renewable Energy Laboratory, Concentrating Solar Power Projects (2020).
URL https://solarpaces.nrel.gov/

[41] National Renewable Energy Laboratory, Concentrating Solar Power Projects (2020).
URL https://solarpaces.nrel.gov/

[42] Y. Qiu, Y. L. He, Z. D. Cheng, K. Wang, Study on optical and thermal performance of a linear Fresnel solar reflector using molten salt as HTF with MCRT and FVM methods, Applied Energy 146 (2015) 162–173. doi:10.1016/j.apenergy.2015.01.135.
URL http://dx.doi.org/10.1016/j.apenergy.2015.01.135

[43] K. Vignarooban, X. Xu, A. Arvay, K. Hsu, A. M. Kannan, Heat transfer fluids for concentrating solar power systems - A review, Applied Energy 146 (2015) 383–396. doi:10.1016/j.apenergy.2015.01.125.
URL http://dx.doi.org/10.1016/j.apenergy.2015.01.125

[44] Eastman Chemical Company, THERMINOL VP-1 heat transfer fluid brochure (2019).
URL https://www.therminol.com/product/71093459?pn=
Therminol-VP-1-Heat-Transfer-Fluid

[45] C. Tzivanidis, E. Bellos, D. Korres, K. Antonopoulos, G. Mitsopoulos, Thermal and optical efficiency investigation of a parabolic trough collector, Case Studies in Thermal Engineering 6 (2015) 226–237. doi:10.1016/J.CSITE.2015.10.005.
URL https://www.sciencedirect.com/science/article/pii/S2214157X15300198

[46] E. Z. Moya, 7 - Parabolic-trough concentrating solar power (CSP) systems, in: K. Lovegrove, W. B. T. C. S. P. T. Stein (Eds.), Woodhead Publishing Series in Energy, Woodhead Publishing, 2012, pp. 197–239. doi:https://doi.org/10.1533/9780857096173.2.197.
URL http://www.sciencedirect.com/science/article/pii/B9781845697693500078

[47] S. A. Channiwala, A. Ekbote, A Generalized Model to Estimate Field Size for Solar-Only Parabolic Trough Plant, Third South African Solar Energy Conference 3 (May) (2015) 283–288.
URL https://repository.up.ac.za/bitstream/handle/2263/49534/Ekbote_Generalized_2015.pdf;sequence=1

[48] H. Hou, Z. Xu, Y. Yang, An evaluation method of solar contribution in a solar aided power generation (SAPG) system based on exergy analysis, Applied Energy 182 (2016) 1–8. doi:10.1016/j.apenergy.2016.08.109.

[49] J. Freeman, N. Blair, D. Guittet, M. Boyd, T. Neises, M. Wagner, S. Janzou, P. Gilman, System Advisor Model (2018).
URL https://sam.nrel.gov/

[50] B.-D. GmbH, D. Band, R. Michalzik, BUDGET OFFER REVISION 3 Solar Steam Generator System PROJECT: SOLANA, Tech. rep., SPX, Ratingen (2009).

[51] M. J. Montes, A. Rovira, M. Muñoz, J. M. Martínez-Val, Performance analysis of an Integrated Solar Combined Cycle using Direct Steam

Generation in parabolic trough collectors, Applied Energy 88 (2011) 3228–3238. doi:10.1016/j.apenergy.2011.03.038.

[52] C. Turchi, Parabolic Trough Reference Plant for Cost Modeling with the Solar Advisor Model (SAM), Tech. Rep. July, National Renewable Energy Laboratory, Golden, CO (2010).
URL http://www.nrel.gov/docs/fy10osti/47605.pdf

[53] Tax-Rates, Utah Property Taxes 2020 (2020).
URL http://www.tax-rates.org/

[54] N. Bailey, Interview With Nathan Bailey from PacifiCorp (2019).

[55] Energysage, Investment tax credit for solar power (2020).
URL https://www.energysage.com/solar/cost-benefit/solar-investment-tax-credit/

[56] C. Ramstein, G. Dominioni, S. Ettehad, L. Lam, M. Quant, J. Zhang, L. Mark, S. Nierop, T. Berg, P. Leuschner, C. Merusi, N. Klein, I. Trim, State and Trends of Carbon Pricing 2019, Tech. Rep. June 2019, World Bank Group, Washington, D.C. (2019).
doi:10.1596/978-1-4648-1435-8.

[57] PacifiCorp IRP Resource Planning, 2019 Integrated Resource Plan, Tech. rep., PacifiCorp, Portland, OR (2019).
URL https://www.pacificorp.com/content/dam/pcorp/documents/en/pacificorp/energy/integrated-resource-plan/2019_IRP_Volume_I.pdf

[58] E. O'Shaughnessy, J. Heeter, J. Cook, C. Volpi, Status and Trends in the US Voluntary Green Power Market (2016 Data), Tech. Rep. TP-6A20-70174, National Renewable Energy Laboratory, Golden, CO (2017).
URL http://www.nrel.gov/docs/fy16osti/65252.pdf

[59] R. Wang, J. Sun, H. Hong, H. Jin, Comprehensive evaluation for different modes of solar-aided coal-fired power generation system under common framework regarding both coal-savability and efficiency-promotability, Energy 143 (2018) 151–167. doi:10.1016/j.energy.2017.10.085.
URL https://doi.org/10.1016/j.energy.2017.10.085

[60] J. Wang, L. Duan, Y. Yang, Z. Yang, L. Yang, Study on the general system integration optimization method of the solar aided coal-fired power generation system, Energy (2019) 660–673doi:10.1016/j.energy.2018.12.054.

[61] R. Zhai, M. Zhao, K. Tan, Y. Yang, Optimizing operation of a solar-aided coal-fired power system based on the solar contribution evaluation method, Applied Energy 146 (2015) 328–334.
doi:10.1016/J.APENERGY.2015.01.140.
URL https:
//www.sciencedirect.com/science/article/pii/S0306261915001853

[62] Y. Wang, J. Xu, Z. Chen, H. Cao, B. Zhang, Technical and economical optimization for a typical solar hybrid coal-fired power plant in China, Applied Thermal Engineering 115 (2017) 549–557.
doi:10.1016/j.applthermaleng.2016.12.132.
URL http://dx.doi.org/10.1016/j.applthermaleng.2016.12.132

[63] N. Quirante, J. A. Caballero, I. E. Grossmann, A novel disjunctive model for the simultaneous optimization and heat integration, Computers & Chemical Engineering 96 (2017) 149–168.
doi:10.1016/J.COMPCHEMENG.2016.10.002.
URL https:
//www.sciencedirect.com/science/article/pii/S009813541630309X

[64] K. Donado, L. Navarro, M. C. G. Quintero, M. Pardo, HYRES: A multi-objective optimization tool for proper configuration of renewable hybrid energy systems, Energies 13 (1). doi:10.3390/en13010026.

URL https://www.engineeringvillage.com/share/document.url?mid=cpx_M401bf34816f7c478574M7e7610178163146&database=cpx

[65] A. Baghernejad, M. Yaghoubi, Exergoeconomic analysis and optimization of an Integrated Solar Combined Cycle System (ISCCS) using genetic algorithm, Energy Conversion and Management 52 (5) (2011) 2193–2203. doi:10.1016/J.ENCONMAN.2010.12.019.
URL https://www.sciencedirect.com/science/article/pii/S0196890410005637

[66] W. Zhong, X. Chen, Y. Zhou, Y. Wu, C. López, Optimization of a solar aided coal-fired combined heat and power plant based on changeable integrate mode under different solar irradiance, Solar Energy 150 (2017) 437–446. doi:10.1016/j.solener.2017.04.049.
URL http://dx.doi.org/10.1016/j.solener.2017.04.049

[67] R. Bravo, D. Friedrich, Two-stage optimisation of hybrid solar power plants, Solar Energy 164 (January) (2018) 187–199. doi:10.1016/j.solener.2018.01.078.

[68] F. Wang, H. Li, J. Zhao, S. Deng, J. Yan, Technical and economic analysis of integrating low-medium temperature solar energy into power plant, Energy Conversion and Management 112 (2016) 459–469. doi:10.1016/j.enconman.2016.01.037.
URL http://dx.doi.org/10.1016/j.enconman.2016.01.037

[69] J. Qin, E. Hu, G. J. Nathan, The performance of a Solar Aided Power Generation plant with diverse "configuration-operation" combinations, Energy Conversion and Management 124 (2016) 155–167. doi:10.1016/j.enconman.2016.07.015.
URL http://dx.doi.org/10.1016/j.enconman.2016.07.015

[70] S. Ong, C. Campbell, P. Denholm, R. Margolis, G. Heath, Land-Use Requirements for Solar Power Plants in the United States, Tech. rep.,

National Renewable Energy Laboratory, Golden, CO (2013).
doi:10.1016/j.rapm.2006.08.004.

[71] U.S. Energy Information Administration, Carbon Dioxide Emissions Coefficients by Fuel (2016).
URL https:
//www.eia.gov/environment/emissions/co2{_}vol{_}mass.php

[72] B. Bernal, L. T. Murray, T. R. Pearson, Global carbon dioxide removal rates from forest landscape restoration activities, Carbon Balance and Management 13 (1). doi:10.1186/s13021-018-0110-8.
URL https://doi.org/10.1186/s13021-018-0110-8

[73] J. Lizana, R. Chacartegui, A. Barrios-Padura, J. M. Valverde, Advances in thermal energy storage materials and their applications towards zero energy buildings: A critical review, Applied Energy 203 (2017) 219–239.
doi:10.1016/j.apenergy.2017.06.008.

[74] B. Xu, P. Li, C. Chan, Application of phase change materials for thermal energy storage in concentrated solar thermal power plants: A review to recent developments, Applied Energy 160 (2015) 286–307.
doi:10.1016/j.apenergy.2015.09.016.

[75] J. Pereira da Cunha, P. Eames, Thermal energy storage for low and medium temperature applications using phase change materials - A review, Applied Energy 177 (2016) 227–238.
doi:10.1016/j.apenergy.2016.05.097.
URL http://dx.doi.org/10.1016/j.apenergy.2016.05.097

[76] S. Flueckiger, Z. Yang, S. V. Garimella, An integrated thermal and mechanical investigation of molten-salt thermocline energy storage, Applied Energy 88 (6) (2011) 2098–2105.
doi:10.1016/j.apenergy.2010.12.031.

[77] Y. Tian, C. Y. Zhao, A review of solar collectors and thermal energy storage in solar thermal applications, Applied Energy 104 (2013) 538–553. doi:10.1016/j.apenergy.2012.11.051.
URL http://dx.doi.org/10.1016/j.apenergy.2012.11.051

[78] J. Wu, H. Hou, Y. Yang, E. Hu, Annual performance of a solar aided coal-fired power generation system (SACPG) with various solar field areas and thermal energy storage capacity, Applied Energy 157 (2015) 123–133. doi:10.1016/j.apenergy.2015.08.022.
URL http://dx.doi.org/10.1016/j.apenergy.2015.08.022

[79] K. S. Reddy, V. Mudgal, T. K. Mallick, Review of latent heat thermal energy storage for improved material stability and effective load management, Journal of Energy Storage 15 (2018) 205–227. doi:10.1016/j.est.2017.11.005.
URL http://dx.doi.org/10.1016/j.est.2017.11.005

[80] A. Kumar, S. K. Shukla, A Review on Thermal Energy Storage Unit for Solar Thermal Power Plant Application, Energy Procedia 74 (2015) 462–469. doi:10.1016/j.egypro.2015.07.728.

[81] A. W. Dowling, T. Zheng, V. M. Zavala, Economic assessment of concentrated solar power technologies: A review, Renewable and Sustainable Energy Reviews 72 (January) (2017) 1019–1032. doi:10.1016/j.rser.2017.01.006.
URL http://dx.doi.org/10.1016/j.rser.2017.01.006

[82] Y. A. Cengel, M. A. Boles, Thermodynamics: An Engineering Approach, 7th Edition, McGraw-Hill, New York, NY, 2011.

[83] Finance Formulas, Loan Payment (2019).
URL https://financeformulas.net/Loan{_}Payment{_}Formula.html

[84] The United States of America Congress, Consolidated Appropriations Act of 2016 (2016).

Appendix A State Properties

Simulating the performance of the simplified model requires multiple input values, relationships, and equations relating to equipment performance or operating behavior of the hardware being modeled. A derivative of the state postulate requires two independent, intensive properties to fix the state of a simple compressible system [82]. Thus, for each state in the representative model, two properties that are independent of each other and do not depend on mass (intensive) must be provided to determine the other properties of interest at that state.

For the model presented in this work, we are particularly interested in the following properties.

- Pressure (P [MPa])
- Temperature (T [K])
- Specific enthalpy (h [kJ kg^{-1}])
- Specific entropy (s [kJ kg^{-1} K^{-1}])
- Steam quality (x) $\frac{m_{vapor}}{m_{total}}$

The information required to obtain these properties can be separated into four categories

1. Correlation provided by user (Table A.1)
2. Process design points
3. Conservation of energy
4. Efficiency

We have selected the HPT 1^{st} stage pressure as the control parameter used to adjust the power generation of the plant. Because this pressure is the independent variable, all correlations (category 1) used to calculate the properties for the simulation of the Hunter plant are related to the HPT 1^{st} stage pressure (Table A.1).

The description of state point values are provided sequentially below beginning with state 1. When the properties of a state are dependent on a process related to a later state, some conditions are introduced out of order.

The pressure at state 1 is equivalent to the condenser operating pressure, provided as a correlation in Table A.1 (category 1). The water in condensers is designed to exit as a saturated liquid, so the second property to fix state 1 is x = 0 (category 2).

The feedwater in the condensate stage of real power plants incrementally increases in pressure as it is heated until it enters the DA. In the simplified model, the condensate stage is assumed to take place at constant pressure ($P_2 = P_3 = P_4$), as opposed to the gradual compression experienced in the real plant. This pressure is approximated using a correlation in Table A.1 for the DA extraction pressure (category 1). The CP is assumed to have a constant isentropic efficiency. The isentropic efficiency of a pump is defined as the ratio of the isentropic work ($\Delta s = 0$) to the actual work. For pumps with an outlet enthalpy (h_e) and inlet enthalpy (h_i), the work done by that pump can be derived from conservation of energy to get Equation A.1.

$$W_{pump} = \dot{m}(h_e - h_i) \tag{A.1}$$

The isentropic efficiency can then be written in terms of the actual work (W_a) and isentropic work (W_s) in Equaion A.2.

$$\eta_{pump} = \frac{W_s}{W_a} = \frac{h_{e,s} - h_i}{h_{e,a} - h_i} \tag{A.2}$$

After finding the isentropic enthalpy of state 2 ($h_{e,s} = h(P_2, s_1)$), the actual enthalpy can be calculated using the isentropic efficiency (Equation A.2), which fixes state 2 (category 4).

The enthalpy of state 3 is determined using the FWH efficiency. This method can be written in terms of states 2, 14, and 15 in Equation A.3 (category 2).

$$h_3 = \frac{\eta_{\mathrm{FWH}}}{\dot{m}_{14}(h_{14} - h_{15})} + h(2) \tag{A.3}$$

State 3 is then fixed knowing h_3 and that $P_3 = P_2$, as stated previously (category 2).

State 4 is a simplified model of the DA used in coal plants to remove air from the feedwater before it enters the boiler. The ideal version of a DA is a mixing chamber. In the case of state 4, condensate stream 3 and FWH drain exit (state 12) enter the chamber at equal pressure and exit at the same pressure ($P_3 = P_4 = P_{12}$, category 2). State 4 is fixed after finding the enthalpy of state 4 using the conservation of energy (category 3). For a steady, open system with no external heating or work interactions, N inlet streams, and M exit streams,

$$\sum_{j}^{M}(\dot{m}_j h_j)_{exit} = \sum_{k}^{N}(\dot{m}_k h_k)_{in} \tag{A.4}$$

and, therefore,

$$h_4 = \frac{1}{\dot{m}_4}\left(\dot{m}_3 h_3 + \dot{m}_{12} h_{12}\right) \tag{A.5}$$

However, h_{12} is still unknown for this process. In order to calculate states 4, 11, and 12, a temperature for state 5 is assumed and used with a correlation for pressure in Table A.1 (category 1) to fix the state. The temperature for state 11 is determined using the Drain Cooler (DC) temperature difference specification for FWHs. The DC approach assumes that the drain of the FWH exits at a specified temperature difference above the feedwater inlet temperature. In the case of the HP FWH, T_{11} can be related to the assumed T_5 using Equation A.6 (category 2).

$$T_{11} = T_5 + DC \tag{A.6}$$

It is assumed that the steam exits the FWH for state 11 at the same pressure as the extraction inlet ($P_{11} = P_{10}$, category 2). State 11 is then fixed and can be used to determine state 12.

It has been identified previously that state 12 is at the same pressure as states 3 and 4. A relationship for the throttling process is useful to fix state 12 (category 3). A general expression for a control volume at steady state with no external heating or work interactions is presented in Equation A.5. Equation A.7 shows the results for a single inlet and exit. Since $\dot{m}_{12} = \dot{m}_{11}$, the enthalpy at

states 11 and 12 are equivalent.

$$\sum_{j}^{M}(\dot{m}_j h_j)_{exit} = \sum_{k}^{N}(\dot{m}_k h_k)_{in} \tag{A.7}$$

State 4 is then fixed as previously described and can be used to evaluate the assumed T_5. The new state 5 is fixed using the boiler feed pump (BFP) efficiency (category 4), as described for state 2 (Equation A.2) and a pressure calculated from a correlation in Table A.1 (category 1). The temperature from the new state 5 is compared to the assumed state. A tolerance of 0.1% is applied for sensitivity when comparing the assumed and calculated state 5 temperatures. The properties of the calculated state 5 are then used to iterate through the calculations for states 4, 11, and 12 until the tolerance requirement is met.

State 6 is calculated assuming a FWH efficiency (η_{FWH}) based on the conservation of energy (category 3). For a FWH, the amount of energy transferred between the streams can be determined by analyzing the heat transfer material, or the space between the extraction and feedwater streams. Since the extracted steam and feedwater heat rates are related by η_{FWH},

$$\eta_{\text{FWH}}\ \dot{m}_{10-11}(h_{10} - h_{11}) = \dot{m}_{5-6}(h_6 - h_5) \tag{A.8}$$

and, therefore,

$$h_6 = h_5 + \eta_{\text{FWH}}\frac{\dot{m}_{10-11}}{\dot{m}_{5-6}}(h_{10} - h_{11}) \tag{A.9}$$

State 6 can then be fixed using Equation A.9 and the pressure, assuming $\eta_{\text{FWH}} \approx 99\%$. Similar to the LP FWH, the feedwater exit is assumed to be at the same pressure as the inlet ($P_6 = P_5$, category 2).

State 7 is at the exit of the boiler. For lack of a model for pressure losses in the boiler, a correlation is provided for the boiler outlet pressure in Table A.1 (category 1). It is assumed that a boiler operates at constant temperature (category 1).

The exhaust or extraction properties from a turbine are dependent on turbine pressure limits and isentropic efficiency. For the example of the HPT exhaust

(state 8), the inlet pressure has already been calculated (P_7). The pressure ratio from the inlet of the HPT to the exhaust varies with P_{s1}, but it is assumed that the pressure ratio from P_{s1} to the HPT exhaust is constant. Since the 1st stage pressure is set for a plant operating condition, the HPT exhaust pressure can be calculated using a constant pressure ratio (category 1).

The isentropic efficiency of an adiabatic turbine is similar to Equation A.2 for compressor efficiency.

$$\eta_{turb} = \frac{W_a}{W_s} = \frac{h_{e,a} - h_i}{h_{e,s} - h_i} \tag{A.10}$$

For a specified turbine efficiency (category 1), the exit state can be fixed by rearranging Equation A.10 to solve for $h_{e,a}$ (category 4).

The boiler reheating is assumed to be a constant pressure process ($P_9 = P_8$, category 2). As discussed previously, the boiler operates at a consistent temperature, thus it is assumed that $T_9 = T_7$ (category 2). As long as the water is not a saturated liquid-vapor mixture, pressure and temperature are independent and state 9 is fixed.

Multiple options for modeling state 10 have been considered; the selected option is to throttle a fraction of the steam extracted from the HPT exhaust to the mass-averaged pressure. The process to calculate the mass-averaged pressure is based on a generalized schematic in Figure A.1.

In the case represented in Figure A.1, there are 3 HP FWHs with a single extraction from the HPT exhaust (A) and 2 extractions from the IPT (B, C). First, the FWH mass fraction (mf) is calculated using a ratio of the respective extraction mass flow rate to the total mass extracted, as in Equation A.11 for the FWH mass fraction of stream A.

$$mf_A = \frac{\dot{m}_A}{\dot{m}_A + \dot{m}_B + \dot{m}_C} \tag{A.11}$$

The mass-averaged pressure is assumed to be the combination of each of the individual extraction pressures (Equation A.12) while the extraction mass flow

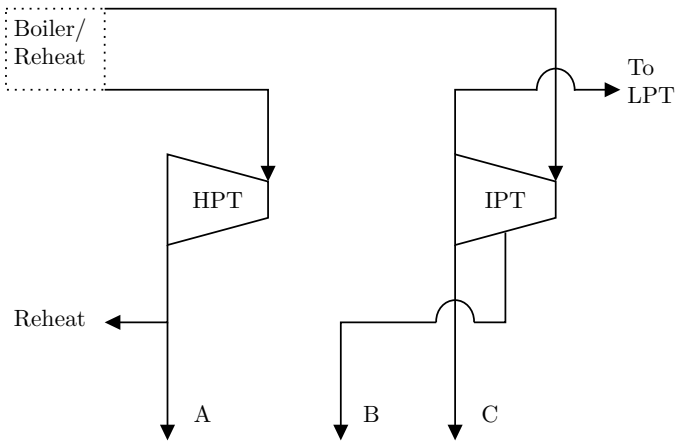

Figure A.1: Generalized schematic to illustrate the process of calculating the mass-averaged pressure used in the simplified model.

rate in the simplified model is assumed to be equal to the sum of the extraction flow rates.

$$P_{mavg} = mf_A P_A + mf_B P_B + mf_C P_C \tag{A.12}$$

This mass-average process is implemented using the correlations for turbine pressure ratios and mass fractions listed in Table A.1 (category 1) to determine the throttling pressure and extraction mass flow rate for state 10 (category 2). State 10 is fixed using the isenthalpic valve assumption as in Equation A.7 (category 3).

The extraction mass flow rate used in the mass-average process is calculated using extraction fractions (m_{ef}). For HP extractions, m_{ef} is the fraction of the mass differential between the main steam flow ($\dot{m}_7$) and the DA inlet ($\dot{m}_3$). The LP m_{ef} are the fractions of the mass flow into the LPT ($\dot{m}_{13}$). Values for m_{ef} are determined by plant operating data.

The pressure at the exit of the IPT (state 13) is specified by a correlation for the IPT pressure ratio in Table A.1 (category 1). The enthalpy for state 13 is determined using the turbine isentropic efficiency (Equation A.10, category 4).

States 14 and 17 are also fixed using exit pressures and the LPT isentropic efficiency (Equation A.10, category 1). The extraction pressure (P_{14}) is assumed to be at the mass-averaged pressure from the real power plant LP FWHs as described in Equation A.12 (category 2). The LPT is assumed to exhaust to the condenser, i.e. $P_{17} = P_1$ (category 2).

States 15 and 16 are determined in the same way as states 11 and 12, using the DC approach (Equation A.6, category 2) at constant pressure ($P_{15} = P_{14}$, category 2) and isenthalpic valve assumption (Equation A.7, category 3) exiting at the condenser pressure ($P_{16} = P_1$, category 2).

In summary, below is a list of inputs the model requires in order to simulate the power plant performance:

- Condenser pressure
- All FWH extraction pressures
- Boiler inlet pressure
- Boiler outlet pressure
- Boiler operating temperature
- Boiler inlet mass flow rate
- DA inlet water mass flow rate
- Extraction fractions for each FWH
- HPT 1st stage-exhaust pressure ratio
- HPT, IPT, LPT isentropic efficiencies
- IPT, LPT extraction pressure ratios

A.1 Correlations

The extraction fraction for the FWH mass flow rates are the amount of mass extracted compared to a design point reference. For the HP extractions, the fractions are constant (FWH 5: 0.19, FWH 6: 0.15, FWH 7: 0.37) and refer to the extraction as compared to the difference between the HPT inlet flow rate and the DA inlet flow rate. The LP extraction fractions are also constant (FWH 1: 0.057, FWH 2: 0.035, FWH 3: 0.037) and refer to the extraction as compared to the LPT inlet flow rate. The performance of the cycle based on the new P_{s1}

is then simulated according to the process outlined above and the conservation of energy constraint is applied to the combined FWHs.

Table A.1: Correlation property equations for use in the representative model. Properties generally follow a power law relationship ($\mathcal{P} = aP_{s1}^{b} + c$) where P_{s1} is in MPa. Constant properties are shown where $a = b = 0$.

Property ($\mathcal{P}$)	P_6 [MPa]	r_{HPT}	$r_{\text{FWH 6}}$	$r_{\text{FWH 5}}$	r_{IPT}	r_{DA}	r_{FWH3}	$r_{\text{FWH 2}}$	r_{LPT}	$\dot{m}_6$ [kg s^{-1}]	$\dot{m}_{DA}$ [kg s^{-1}]	T_B [K]	P_{cond} [MPa]	η_{HPT} [%]	η_{IPT} [%]	η_{LPT} [%]
a	2.9985	10.7684	0	-0.7076	0	49.7939	0	0	0	31.3897	25.5728	0	0	0	0	0
b	0.548	0.1739	0	-0.8261	0	-3.4562	0	0	0	1	1	0	0	0	0	0
c	7.6221	0	1.8155	2.6838	2.5860	2.2131	5.7824	13.0703	62.65	0.75	-2.7841	811.8	8.1e-3	89.4	91.7	91.8

Appendix B Financial Parameters

This Appendix provides the information required to use the values presented in Table 4 to calculate capital costs and annual costs for the cash flow analysis. As noted in the main body of this work, the financial model was developed to replicate the NREL Solar Advisor Model (SAM) [49]. Similarly, in this supplemental material, equations are obtained from SAM documentation unless otherwise noted. All cost values calculated using the equations in this section are added to approximate the overall capital and annual costs to be used in Equation 9 to calculate LCOE or as part of the cash flow analysis to estimate PBT.

B.1 Capital Costs

Overall capital costs use the factors and rates itemized in Table 4. More specifically, the different direct and indirect costs are listed in Table B.1 along with the equation to calculate each cost.

B.2 Operating and Maintenance (O&M) Expenses

Annual O&M expenses (C_{exp}) include fixed (C_{FOM}) and variable (C_{VOM}) O&M costs, insurance (C_{ins}), and property tax ($C_{t,prp}$). The total expenses for each year are the sum of the previously mentioned cost values as shown in Equation B.1.

$$C_{exp} = C_{\mathrm{FOM}} + C_{\mathrm{VOM}} + C_{ins} + C_{t,prp} \tag{B.1}$$

B.3 Loan Payments

Annual loan payments are a constant yearly payment that are equal to the sum of the debt interest and the principle payment. Equation B.2 calculates the principle and interest payment ($C_{P\&I}$) from the loan rate (r_{int}), initial loan balance ($L_{net,0}$), and loan period (N_L) [83].

$$C_{\mathrm{P\&I}} = \frac{r_{int} \cdot L_{net,0}}{1 - (1 + r_{int})^{N_L}} \tag{B.2}$$

Table B.1: Methods used to calculate the capital cost.

Cost item	Variable	Calculation method [USD]
Direct Costs ($C_{\mathbf{DC}}$)		
Site improvements	C_{SI}*	$C_{\mathrm{SI}} = F_{\mathrm{SI}} A_p$
Solar field	C_{SF}†	$C_{\mathrm{SF}} = F_{\mathrm{SF}} \cdot A_p$
HTF system	C_{HTF}‡	$C_{\mathrm{HTF}} = F_{\mathrm{HTF}} \cdot A_p$
Heat exchanger	C_{HX}§	$C_{\mathrm{HX}} = F_{\mathrm{HX}} \cdot 1000000$
Contingency	C_{cont}	$C_{cont} = r_{cont}(C_{\mathrm{SI}} + C_{\mathrm{SF}} + C_{\mathrm{HTF}} + C_{\mathrm{HX}})$
Total direct costs	C_{DC}	$C_{\mathrm{DC}} = C_{\mathrm{SI}} + C_{\mathrm{SF}} + C_{\mathrm{HTF}} + C_{\mathrm{HX}} + C_{cont}$
Indirect Costs ($C_{\mathbf{IC}}$)		
EPC and owner costs	C_{EPC}	$C_{\mathrm{EPC}} = r_{\mathrm{EPC}} \cdot C_{\mathrm{DC}}$
Sales tax	$C_{t,sal}$	$C_{t,sal} = r_{t,sal} \cdot F_{t,sal} \cdot C_{\mathrm{DC}}$
Total indirect costs	C_{IC}	$C_{\mathrm{IC}} = C_{\mathrm{EPC}} + C_{t,sal}$
Total Capital Cost	CC	$\mathrm{CC} = C_{\mathrm{DC}} + C_{\mathrm{IC}}$

*C_{SI}: Costs for site preparation and other expenses not included in the solar field.
†C_{SF}: Costs related to the installation and purchase of parts related to the solar field.
‡C_{HTF}: Costs accounting for installation of pumps and piping of HTF system, including labor and equipment.
§C_{HX}: Costs accounting for the installation and purchase of a heat exchanger.

B.4 Tax Credits

Tax credits are an important variable when considering renewable energy sources. This study focuses primarily on the federal Investment Tax Credit (ITC) and Project Tax Credit (PTC). Other incentives used in the SAM financial model but not included in this study are: Investment based incentives, capacity based incentives, and production based incentives [49]. These incentives were omitted because there is no recent history of them being applicable for CSP in the United States.

ITC is a percentage of the investment for solar energy equipment, and is included in the tax refund for the year the investment was made. Equation B.3 shows the calculation of the ITC based on the capital cost and the ITC rate

(r_{ITC}).

$$\text{ITC} = \text{CC} \cdot r_{\text{ITC}} \tag{B.3}$$

The PTC is less relevant for this study since the Consolidated Appropriations Act of 2016 terminated the federal PTC for solar power generation [84]. However, Equation B.4 demonstrates how to calculate the federal PTC, in the case that it is reinstated, or if a similar program is applicable in other countries, by using the PTC rate (r_{PTC}), the electrical capacity of the solar augmentation ($\dot{W}sol$) and the amount of hours in a year. The PTC is only applied throughout a government specified term.

$$\text{PTC}_n = 365\ \dot{W}_{sol}\ r_{\text{PTC}}\ h_{sun} \tag{B.4}$$

ITC is included in the income tax savings during the first year of the project. PTC is included in the income tax savings during the duration of time specified by the applicable tax law.

B.5 Income Tax

Once the operating expenses, loan payment, and tax credits have been determined, it is then possible to calculate the federal and state income taxes. The calculation for both the federal and the state income taxes are almost identical, however, the state income tax is calculated before the federal income tax so that the state tax will be considered when calculating federal deductions.

Income taxes, including income tax savings (S_t), are based on state and federal income tax rates, depreciation schedule, taxable income, operating expenses, interest payments, and applicable tax credits. The method for calculating each value may also vary depending on project location. Once calculated, Equation B.5 shows that S_t is equal of the sum of ITC, PTC (where applicable), and federal ($S_{t,Fed}$) and state ($S_{t,st}$) income tax savings.

$$S_t = S_{t,Fed} + S_{t,st} + \text{ITC} + \text{PTC} \tag{B.5}$$

B.6 After Tax Costs

After calculating the operating expenses, loan payment, tax credits, and income taxes, C_{tot} can then be determined for each year as shown in Equation B.6.

$$C_{tot} = C_{exp} + C_{\text{P\&I}} - S_t \tag{B.6}$$

The total capital costs for each year ($C_{tot,n}$) can then be used in Equation 8 to calculate C_{net} which is then used in Equation 9 to calculate LCOE.